RSC Advances

PAPER

View Article Online
View Journal | View Issue



Cite this: *RSC Adv.*, 2026, **16**, 9475

# Anaerobic pyrolysis of textile garment waste for the production of multifunctional biochar: fuel performance and Pb(II) and Cr(VI) adsorption with machine learning prediction

Thu Huong Nguyen,[a] Trung Kien Hoang,[a] Huu-Tap Van [b] and Thi Minh Phuong Nguyen *[cd]

The rapid growth of the textile and garment industry generates large quantities of solid waste and heavy-metal-contaminated wastewater, creating coupled environmental challenges that require integrated solutions. In this study, post-industrial garment waste was valorized into a multifunctional carbon material *via* anaerobic pyrolysis and evaluated for dual applications as a solid fuel and as an adsorbent for simultaneous Pb(II) and Cr(VI) removal from aqueous solutions. Carbonized garment waste biochars (CGW) were produced at 400–900 °C and characterized by SEM, EDX, XRD, FTIR and BET analyses. Carbonization temperature strongly influenced surface chemistry, pore structure, and functionality. CGW600 exhibited the highest surface area (56.85 $m^2\ g^{-1}$) and pore volume (0.046 $cm^3\ g^{-1}$), whereas CGW800–900 showed superior fuel properties with high carbon content (>76 wt%), low ash (<1.4 wt%), and high calorific values (6906–7069 kcal $kg^{-1}$). CGW600 achieved maximum adsorption capacities of 23.18 mg $g^{-1}$ for Pb(II) and 19.68 mg $g^{-1}$ for Cr(VI), with effective simultaneous removal at pH 7 (9.43 ± 0.26 and 8.78 ± 0.18 mg $g^{-1}$, respectively). Spectroscopic evidence and modeling indicate adsorption dominated by surface complexation and ion exchange, with additional redox-assisted interactions for Cr(VI). Machine learning analysis ($R^2$ = 0.99 for Pb; 0.987 for Cr) identified pH, adsorbent dosage and initial concentration as key controlling factors. The present results outline a temperature-dependent methodology for upcycling textile waste into advanced carbon materials with dual applicability in energy generation and aqueous pollutant removal. Such an integrated framework advances sustainable material development and contributes to effective strategies for environmental cleanup and reduced waste burden.

Received 15th January 2026
Accepted 11th February 2026

DOI: 10.1039/d6ra00384b

rsc.li/rsc-advances



## Introduction

The global textile and garment industry has experienced rapid growth over recent decades, accompanied by a substantial increase in solid waste generation, particularly post-industrial garment scraps and off-cuts. Current estimates indicate that more than 90 million tonnes of textile waste are produced annually worldwide, with over two-thirds disposed of in landfills or incinerated, leading to environmental burdens, greenhouse gas emissions, and the loss of carbon-rich resources.[1,2] In rapidly industrializing countries such as Vietnam, where textile manufacturing represents a major economic sector, garment waste management remains largely disposal-oriented, with limited implementation of resource recovery or circular economy strategies.[3]

Biochar derived from biomass waste has been widely investigated as a low-cost, sustainable material for environmental remediation, owing to its porous structure, surface functional groups, and tunable physicochemical properties. Previous studies have demonstrated the effectiveness of biochar in adsorbing organic dyes, pharmaceuticals, and heavy metals, as well as its role as a functional support in advanced remediation systems. For example, pomegranate peel – derived biochar exhibited high adsorption capacity for malachite green *via* surface adsorption and pore-filling mechanisms, highlighting the potential of agricultural waste valorization for pollutant removal.[4] Beyond conventional adsorption, recent studies have expanded the role of biochar to multifunctional environmental applications. Biochar has been employed as a conductive support to enhance charge transfer in photocatalytic systems, enabling synergistic adsorption–degradation pathways for recalcitrant pollutants. For instance, Rheum ribes waste-

[a]*Faculty of Natural Resources and Environment, TNU – University of Sciences, Thai Nguyen 24000, Vietnam*

[b]*Center for Advanced Technology Development, Thai Nguyen University, Thai Nguyen 24000, Vietnam*

[c]*Faculty of Environmental and Natural Sciences, Duy Tan University, Da Nang 550000, Vietnam. E-mail: nguyentminhphuong@dtu.edu.vn*

[d]*Institute of Research and Development, Duy Tan University, Da Nang 550000, Vietnam*

derived biochar-supported $Bi_2MoO_6$ nanocomposites exhibited efficient charge separation and visible-light-driven antibiotic degradation, underscoring biochar's role in facilitating electron transport and interfacial reactions.[5] In parallel, biochar has also been integrated into biological and hybrid remediation strategies. It has been reported as an effective carrier for plant growth-promoting bacteria in phytoremediation systems, thereby improving microbial survival, pollutant immobilization, and remediation efficiency.[6] Furthermore, nanobioremediation approaches combining microorganisms with nanostructured materials have been proposed to enhance metal immobilization, redox transformations, and detoxification, particularly under complex environmental conditions.[7]

Thermochemical conversion, particularly anaerobic pyrolysis, has emerged as an effective route for valorizing textile waste into value-added products such as biochar, syngas, and bio-oil.[8] Pyrolysis reduces waste volume and toxicity while enabling energy recovery and material reuse, supporting sustainable waste management and circular economy concepts.[9–11] Carbonized textile-derived[12] materials typically exhibit high fixed carbon content and low ash content, making them suitable for solid-fuel applications.[13] Several studies have reported that textile- and polymer-containing wastes can be converted into chars with calorific values comparable to or exceeding those of conventional coal-based fuels, indicating potential for household and small-scale industrial energy use.[14] Elevated carbonization temperatures, while improving fuel quality, can induce structural densification and reduce surface functionality, which limits environmental remediation performance.

Biochar has also been extensively investigated as an adsorbent for heavy metal removal from aqueous systems. Its adsorption performance depends on surface chemistry, pore structure, and mineral composition, which are strongly influenced by feedstock characteristics and pyrolysis conditions.[15] Most studies have focused on agricultural residues and forestry biomass, whereas the conversion of actual garment waste – often containing cotton–polyester blends, dyes, and finishing additives – into multifunctional biochar remains underexplored. The heterogeneous composition of garment waste can significantly affect both combustion behavior and adsorption mechanisms.

Most existing studies treat biochar either as a fuel or as an adsorbent, with limited consideration of its dual functionality. Integrating energy recovery with wastewater treatment could improve the technical and economic feasibility of textile waste valorization. Carbonized garment waste-derived biochar (CGW), for example, could be used as a cooking or heating fuel. In contrast, the same material, whether used before or after partial utilization, could serve as an adsorbent for heavy metal removal. Achieving this multifunctionality requires optimization of carbonization conditions to balance fuel-related properties, such as calorific value, ash content, and combustion stability, with adsorption-related properties, including surface area, functional groups, and pore accessibility.

A further knowledge gap concerns the simultaneous removal of Pb(II) and Cr(VI) under environmentally relevant conditions. Pb(II) adsorption is generally favored at neutral to alkaline pH through electrostatic attraction and surface complexation, whereas Cr(VI) removal is often most efficient under acidic conditions due to enhanced electrostatic attraction and reduction to Cr(III).[16] In practical wastewater treatment, extreme pH adjustment is undesirable, and operation near neutral pH is preferred.[17] As a result, the mechanistic understanding of Pb–Cr co-removal at near-neutral pH using waste-derived biochars remains limited.

Classical kinetic and isotherm models may not fully capture the non-linear interactions among process variables such as pH, adsorbent dosage, contact time, initial concentration, and material properties. Machine learning approaches, including artificial neural networks, random forests, and support vector machines, have shown strong potential for predicting adsorption performance and identifying dominant controlling factors in complex environmental systems.[18] Their application to mixed-metal adsorption systems using textile waste-derived biochars, particularly in conjunction with fuel performance evaluation, remains scarce.

Recent advances have demonstrated that biomass-derived carbon materials (including biochar-like frameworks) can be engineered with tailored surface chemistry and functionality, enabling high performance not only in adsorption but also in catalysis and sustainable energy conversion. For instance, Huang *et al.* reported a lignin-derived layered 3D biochar with controllable acidity, highlighting how rational tuning of acid/base sites and microstructure can markedly enhance functional performance in catalytic upgrading processes.[19] In a related direction, Huang *et al.* developed a graphene-like biomaterial-based system anchored with neighboring potassium single atoms, achieving efficient biodiesel production under mild conditions and demonstrating the growing capability of bio-derived carbon platforms to deliver advanced, highly active functional sites while aligning with carbon-negative or low-carbon concepts.[20] Despite this progress, an integrated assessment that simultaneously valorizes real post-industrial garment waste into a multifunctional carbon material for solid-fuel performance and simultaneous Pb(II)/Cr(VI) removal at near-neutral pH, combined with machine-learning-based prediction, remains limited. Therefore, the present study advances the field by providing a unified framework that couples textile-waste-to-energy valorization with wastewater remediation using a single waste-derived carbon material.

Despite these advances, several critical gaps remain. Most existing studies focus on a single biochar functionality, such as adsorption or catalytic support, without considering trade-offs between energy recovery and environmental remediation. In addition, most adsorption studies are conducted under tightly controlled conditions, limiting their relevance to real-world scenarios where multiple contaminants coexist at environmentally relevant pH values. Moreover, the valorization of post-industrial textile waste into multifunctional carbon materials remains underexplored. To address these gaps, the present study converts post-industrial garment waste into a multifunctional biochar *via* anaerobic pyrolysis. It systematically evaluates its dual performance as a solid fuel and as an adsorbent for

 

the simultaneous removal of Pb(II) and Cr(VI) from aqueous solutions. The effects of carbonization temperature on material properties, energy performance, adsorption behavior, and underlying mechanisms are elucidated through comprehensive characterization and machine-learning analysis.

It is hypothesized that the carbonization temperature of post-industrial garment waste is a critical process parameter that governs the multifunctional performance of the resulting biochar, thereby generating an intrinsic trade-off between its fuel properties and adsorption capacity. Specifically, fixed carbon content, higher heating value (calorific value), and combustion stability are expected to be increased when higher carbonization temperatures are applied, whereas greater specific surface area and a higher density of surface oxygen-containing functional groups – particularly favorable for Pb(II) and Cr(VI) adsorption – are anticipated to be preserved at moderate carbonization temperatures. Although simultaneous maximization of both energetic performance and heavy metal adsorption efficiency in a single biochar sample is unlikely, it is proposed that a practically viable balance can be achieved through careful optimization of the carbonization temperature, enabling integrated applications in waste-derived energy recovery and wastewater remediation.

## Materials and methods

This section describes the experimental design, material preparation, characterization techniques and analytical methods employed to evaluate the CGW as both a solid fuel and an adsorbent. The methodological framework was designed to systematically investigate how carbonization temperature governs the trade-off between energy recovery and adsorption performance, thereby enabling the establishment of a structure–property–function relationship.

### Chemicals

Lead nitrate ($Pb(NO_3)_2$, ≥99.0% purity, Sigma-Aldrich) and potassium dichromate ($K_2Cr_2O_7$, ≥99.5% purity, Merck) were used as Pb(II) and Cr(VI) sources, respectively. Nitric acid ($HNO_3$, 65%, Merck) and sodium hydroxide (NaOH, ≥98%, Sigma-Aldrich) were employed for pH adjustment. All chemicals were of analytical grade and used as received without further purification. Deionized water was used throughout the experiments.

A synthetic wastewater solution was prepared to simulate effluents from textile dyeing and finishing operations. The simulated solution contained lead ($Pb^{2+}$) and chromium ($Cr^{6+}$) ions, introduced as $Pb(NO_3)_2$ and $K_2Cr_2O_7$, respectively. A stock solution of 1000 mg $L^{-1}$ was prepared for each metal, and subsequent working solutions were obtained by serial dilution to concentrations ranging from 50 to 500 mg $L^{-1}$. These controlled solutions were used to systematically evaluate the biochar's adsorption capacity and removal efficiency under varying physicochemical conditions, including pH, temperature and contact time.

### Preparation of adsorption material from garment waste *via* anaerobic pyrolysis

The CGW was synthesized *via* anaerobic pyrolysis, a thermochemical decomposition process conducted in the absence of oxygen, thereby converting textile waste into high-value biochar. The complete experimental workflow is detailed as follows.

**Feedstock preparation.** The garment waste used as the carbonaceous precursor was collected from the Thanh Hung garment factory (Thai Nguyen, Vietnam). The waste primarily consisted of discarded fabrics and off-cuts generated during garment manufacturing, with a predominant composition of cotton fibers blended with polyester. Prior to carbonization, the textile waste samples were manually sorted to remove non-fabric contaminants, such as metals, plastics and dyes, thoroughly washed to eliminate surface impurities, and air-dried under ambient conditions to ensure moisture removal. The cleaned and dried samples were then stored in sealed containers until use in the pyrolysis process.

**Pyrolysis reactor design and configuration.** Carbonization of garment waste was performed in a custom-engineered vertical anaerobic pyrolysis reactor developed by the research team. The system was designed to achieve high thermal efficiency and low emissions, while enabling controlled conversion of garment waste into carbon-rich biochar with dual applications: as a solid fuel and as an adsorbent for water treatment. Details on the reactor design, configuration, and operational description are provided in the SI to support the main findings of this study (see SI-1 and Fig. S1 for details).

Fig. S1 illustrates the schematic design and operational configuration of the reactor. The system features an upper loading door for introducing pre-dried garment waste and a lower discharge port for biochar collection after cooling. The recirculating gas pipeline ensures uniform heat distribution, while the insulated vertical structure maintains the anaerobic environment required for efficient carbonization. This configuration enables energy recovery from volatile gases, minimizes greenhouse gas emissions, and yields high-quality biochar optimized for both energy and environmental remediation purposes.

The diagram presents the engineering layout of the custom-built reactor used to CGW. Constructed from stainless steel with refractory insulation, the system includes a primary liquefied petroleum gas burner, an organic vapor recirculation loop for heat recovery, an exhaust gas outlet, and a temperature control network. This configuration ensures efficient, oxygen-limited pyrolysis, enabling the production of high-carbon biochar with dual utility as both a clean-burning fuel and an adsorbent for wastewater purification.

**Pyrolysis procedure.** Pre-dried garment waste feedstock was loaded into the reactor and pyrolyzed at 4 controlled temperatures – 400 °C, 600 °C, 800 °C and 900 °C – with a holding time of 2 hours per run. The biochar was produced at carbonization temperatures ranging from 400 to 900 °C to systematically investigate the temperature-dependent evolution of material properties and their implications for multifunctional performance. This temperature range was selected to capture the

transition from incomplete carbonization and functional-group-rich surfaces at lower temperatures to highly carbonized structures with enhanced fixed carbon content and calorific value at higher temperatures. Such a design enables direct evaluation of the trade-off between fuel-related properties (*e.g.*, fixed carbon, ash, and calorific value) and adsorption-related properties (*e.g.*, surface area, pore structure, and surface functional groups). The heating rate was maintained at approximately 5–10 °C $min^{-1}$ to ensure uniform thermal degradation of the material. Under anaerobic conditions, the garment waste underwent sequential decomposition reactions, yielding solid biochar, combustible gases (CO, $H_2$, $CH_4$, light hydrocarbons), and a small fraction of bio-oil. The generated vapors were continuously redirected into the combustion chamber to sustain the heating process, thus enhancing the overall energy efficiency of the system.

**Post-pyrolysis treatment.** After pyrolysis completion, the system was allowed to cool naturally to ambient temperature to prevent oxidation and structural collapse of the biochar. The resulting carbonized products were washed with deionized water to remove ash and soluble residues, then dried in a Joytech ON-21E oven at 105 °C for 2 hours to obtain a stable, low-moisture biochar. The produced samples were labeled according to their carbonization temperatures: CGW400, CGW600, CGW800 and CGW900.

**Characterization of CGW.** The physicochemical properties of the CGW samples were comprehensively evaluated to assess their suitability as solid fuels and adsorbents. The primary analytical parameters included carbon content, volatile matter, ash content, moisture content and calorific value. Morphological and elemental analyses were performed using XRD, SEM and EDX to examine surface texture, porosity and elemental distribution. These analyses provided insight into the effects of carbonization temperature on pore structure formation, surface chemistry, and adsorption behavior of the garment waste-derived biochars.

**Fuel performance testing of CGW.** The fuel performance of the CGW samples was experimentally assessed to evaluate their potential as an alternative solid fuel. Four types of biochar – CGW400, CGW600, CGW800, and CGW900 – corresponding to pyrolysis temperatures of 400, 600, 800 and 900 °C, respectively, were tested under identical conditions.

For each test, 0.5 kg of CGW was placed in a domestic coal stove, and 1 L of tap water ($\approx$1 kg) at 22 °C was poured into a 3 L aluminum pot. The pot was positioned directly above the burning biochar, and the boiling performance test was initiated. Key performance metrics, including time required to reach boiling point, total combustion duration, residual water volume after complete fuel burnout, thermal efficiency, and specific fuel consumption, were recorded.

For comparative evaluation, commercial honeycomb coal briquettes were tested following the same procedure. All measurements were repeated in triplicate, and the average values were used for subsequent analysis. This comparison enabled the assessment of the thermal output, combustion stability, and energy conversion efficiency of CGW relative to conventional household fuel.

**Adsorption experiments for Pb(II) and Cr(VI) removal.** Pb(II) and Cr(VI) were selected as representative target contaminants because they are among the most toxic and frequently detected heavy metals in effluents from textile, electroplating, tanning, and pigment industries. These two metals commonly coexist in industrial wastewater but exhibit fundamentally different chemical behaviors: Pb(II) is typically removed through surface complexation and ion exchange, whereas Cr(VI) exists as oxyanions and may undergo adsorption coupled with reduction to Cr(III). Investigating Pb(II) and Cr(VI) simultaneously therefore provides a stringent test of the adsorption versatility and mechanistic robustness of the biochar materials. To assess the adsorptive capacity of the CGW, a series of batch adsorption experiments was conducted using synthetic wastewater containing Pb(II) and Cr(VI) ions. The stock solutions were prepared from $Pb(NO_3)_2$ and $K_2Cr_2O_7$, each at an initial concentration of 20 mg $L^{-1}$ and subsequently diluted to the desired concentrations for the experimental runs.

All adsorption experiments were performed under controlled batch conditions, systematically investigating the effects of carbonization temperature (400–900 °C), solution pH (3–11), adsorbent dosage (0.01–1.0 g/25 mL), contact time (5–240 min) and initial metal concentration (10–100 mg $L^{-1}$). The suspensions were agitated using a horizontal shaker (HY-4A, China) at 120 rpm to ensure uniform mixing. After each run, the samples were filtered, and the residual metal ion concentrations were quantified using atomic absorption spectrophotometry. Each experiment was conducted in triplicate, and mean values were used for data interpretation.

The adsorption capacity ($q_e$, mg $g^{-1}$) of CGW was calculated based on the concentration difference between initial and equilibrium states. The obtained data were fitted to kinetic models (pseudo-first-order, pseudo-second-order and Elovich) and isotherm models (Langmuir, Freundlich, and Sips) to elucidate the underlying adsorption mechanisms.

**Specific experimental conditions.** To systematically evaluate the adsorption behavior of Pb(II) and Cr(VI) onto CGW, a series of batch experiments was conducted under controlled conditions. The effect of pyrolysis temperature was first examined by adding 0.20 g of CGW produced at different carbonization temperatures (400–900 °C) into 50 mL conical flasks containing 25 mL of a mixed Pb–Cr solution with an initial concentration of 100 mg $L^{-1}$ at pH 9. This alkaline pH was intentionally selected at the screening stage to minimize competition from protonation effects and to promote electrostatic attraction between negatively charged biochar surfaces and metal species, thereby enabling clearer differentiation of adsorption performance among CGW samples produced at different carbonization temperatures. Such conditions allow the intrinsic influence of pyrolysis temperature on adsorption capacity to be evaluated without the confounding effects of pH-dependent surface chemistry. The suspensions were agitated at 120 rpm for 90 min to ensure sufficient contact between the adsorbent and the metal ions. Subsequently, the influence of solution pH on adsorption performance was investigated by mixing 0.05 g of CGW (400–900 °C) with 25 mL of a Pb(II)–Cr(VI) solution

containing 10 mg $L^{-1}$. The solution pH was adjusted to 3, 5, 7, 9 and 11 using dilute $HNO_3$ or NaOH, and the mixtures were shaken for 60 min to reach equilibrium. The effect of adsorbent dosage was evaluated by varying the amount of CGW from 0.01 to 1.0 g in 25 mL of a 10 mg $L^{-1}$ Pb–Cr mixed solution at the previously determined optimal pH, while maintaining a constant contact time of 60 min. To elucidate adsorption kinetics, the optimal biochar dosage determined in the dosage experiments was applied and the suspensions were agitated for 5–240 min. The contact time was varied from 5 to 240 min to distinguish rapid surface adsorption from slower intraparticle diffusion-controlled stages. Aliquots were withdrawn at predetermined time intervals to determine time-dependent metal uptake. Finally, the effect of initial metal concentration was assessed by contacting the optimized CGW dosage with 25 mL of Pb–Cr solutions at initial concentrations of 10–100 mg $L^{-1}$ at the optimal pH, with a fixed contact time of 90 min. The experimental data obtained from these investigations were subsequently used to develop kinetic, equilibrium isotherm, and machine-learning-based predictive models describing the adsorption behavior of Pb(II) and Cr(VI) onto CGW, as discussed in the following sections.

**Adsorption kinetic and isotherm models.** The adsorption performance of Pb(II) and Cr(VI) ions onto the CGW was quantitatively analyzed using kinetic and isotherm models to elucidate the governing mechanisms of mass transfer and surface interactions.

The adsorption capacity of CGW at a specific contact time ($q_t$, mg $g^{-1}$) and at equilibrium ($q_e$, mg $g^{-1}$) was determined using eqn (1)–(8) in SI-2 of the SI.

To investigate the adsorption rate and mechanism, the kinetic data were fitted using three established models: the pseudo-first-order, pseudo-second-order and Elovich models. Equilibrium adsorption data for Pb(II) and Cr(VI) were further analyzed using three classical isotherm models – Langmuir, Freundlich, and Sips – to describe the interactions between the metal ions and the heterogeneous surface of CGW.

The Langmuir model assumes monolayer adsorption onto a homogeneous surface, whereas the Freundlich model describes multilayer adsorption on heterogeneous surfaces. The Sips isotherm, a hybrid of the two, effectively reduces to the Langmuir model at low solute concentrations and to the Freundlich model at high solute concentrations, thereby providing a comprehensive description of both uniform and non-uniform adsorption sites.

**Machine learning modeling.** Artificial neural networks (ANN), random forests (RF), linear regression (LR) and support vector machines (SVM) were employed to analyze and predict adsorption performance, as these algorithms are well-suited for capturing non-linear relationships among multiple interacting variables. In adsorption systems involving heterogeneous materials and competing mechanisms, classical kinetic and isotherm models may not fully describe the complex dependence on pH, adsorbent dosage, contact time and initial concentration. The combined use of ANN, RF, LR and SVM allows both predictive accuracy and comparative assessment of variable importance, thereby providing complementary insights into the governing factors controlling Pb(II) and Cr(VI) adsorption.

To enhance the predictive accuracy of adsorption behavior and minimize experimental effort, machine learning (ML) models were developed to forecast the adsorption capacity of Pb(II) and Cr(VI) ions on CGW. All model construction and evaluation were performed using R software (version 4.3.1, R Core Team, 2024) within the RStudio environment.[21]

The dataset comprised 128 experimental observations, including five independent input variables – carbonization temperature (Temp., °C), solution pH (pH), adsorbent dosage (Ads_dos, g), initial metal ion concentration (Pb_con or Cr_con, mg $L^{-1}$) and contact time (time, min) – and one dependent target variable: adsorption capacity ($q_e$, mg $g^{-1}$). Detailed information on the machine learning models is provided in Section SI-3 of the SI.

This machine learning framework provides a robust, data-driven methodology for predicting adsorption behavior, significantly reducing the need for extensive laboratory experimentation while enabling rapid optimization of process conditions for heavy metal removal using CGW.

## Results and discussion

### Characteristics of CGW

**Physicochemical properties of CGW.** Fig. 1 shows the SEM images of CGW produced by anaerobic pyrolysis at different carbonization temperatures (400–900 °C), revealing a clear temperature-dependent evolution in surface morphology and structural organization.

At 400 °C (CGW400, Fig. 1a), the biochar retains a fibrous morphology inherited from the original textile precursor, consisting mainly of elongated and intertwined carbonized fibers. This structure indicates incomplete carbonization, where thermal degradation of cotton-dominant fibers occurs without substantial collapse of the polymeric framework. The relatively smooth surface and limited pore development suggest insufficient devolatilization, a characteristic of low-temperature pyrolysis of lignocellulosic and textile wastes.[22,23] Increasing the carbonization temperature to 600 °C (CGW600, Fig. 1b) leads to partial destruction of the fibrous structure and the formation of irregular, fractured carbon domains with rough surfaces and visible cracks. This morphological transition reflects enhanced release of volatile matter and progressive depolymerization and condensation reactions, leading to a more heterogeneous, carbon-enriched matrix. Similar structural transformations have been widely reported for biochars derived from textile and biomass wastes at intermediate pyrolysis temperatures.[24,25] At 800 °C (CGW800, Fig. 1c), the biochar exhibits a well-developed porous structure composed of fragmented carbon blocks with abundant cavities and surface irregularities. The pronounced surface roughness and interconnected pore features indicate extensive devolatilization and structural rearrangement under high-temperature anaerobic conditions. This morphology is highly favorable for mass transfer and adsorption processes, providing a structural basis for the enhanced Pb(II) and Cr(VI) adsorption capacity and

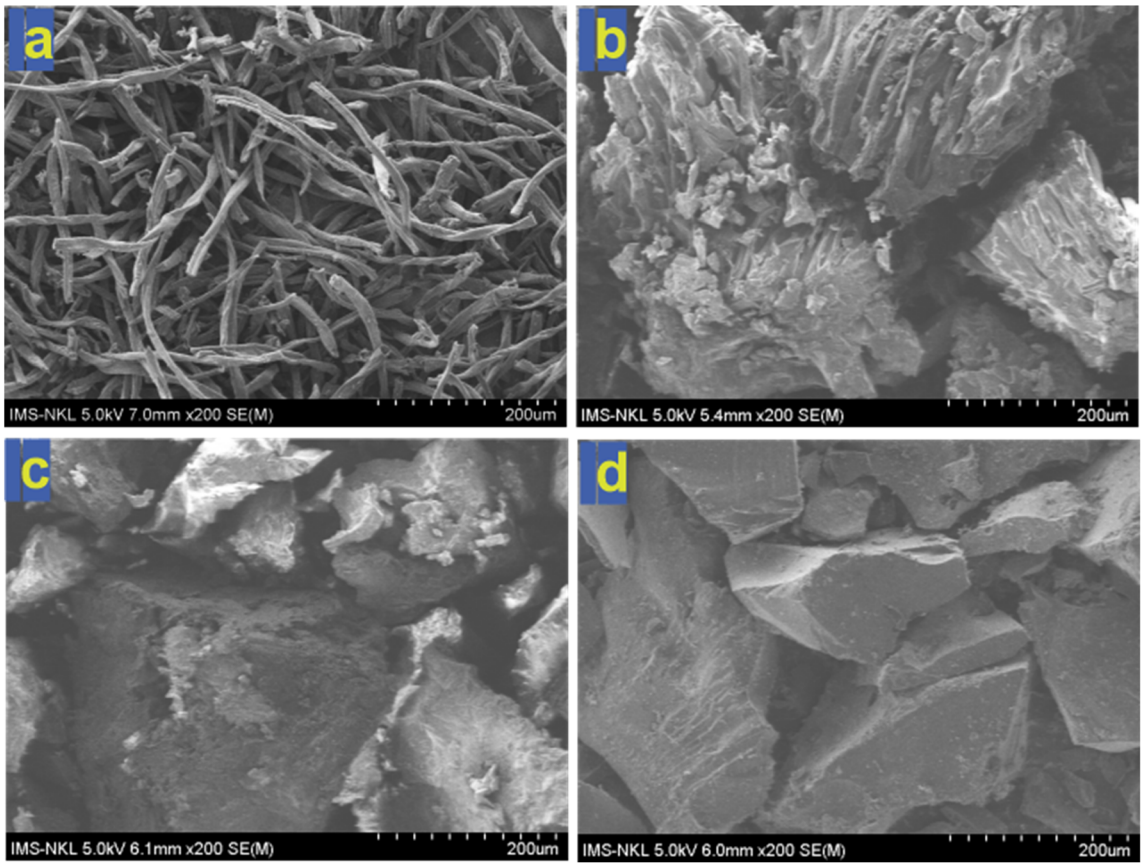


Fig. 1 SEM image of CGW at 400 °C (a), 600 °C (b), 800 °C (c) and 900 °C (d).

improved fuel performance observed for CGW800, consistent with previous reports on high-temperature biochars. Further increasing the carbonization temperature to 900 °C (CGW900, Fig. 1d) results in denser and more compact carbon agglomerates with relatively smoother surfaces and fewer accessible pores. Although higher temperatures promote increased carbon content and structural ordering, excessive thermal severity can induce partial pore collapse and densification due to sintering and fusion of carbon domains, thereby limiting the availability of adsorption-active sites. This phenomenon explains the marginal performance improvement of CGW900 compared to CGW800, despite its higher degree of carbonization.[22,26]

Fig. 2 presents the EDX spectra and elemental compositions CGW obtained *via* anaerobic pyrolysis at carbonization temperatures of 400, 600, 800, and 900 °C, providing insight into the temperature-dependent evolution of surface chemical composition. For CGW400 (Fig. 2a), the EDX spectrum is dominated by carbon (C, ~76 wt%) and oxygen (O, ~24 wt%), reflecting incomplete carbonization of the textile precursor at low temperature. The relatively high oxygen content indicates the persistence of oxygen-containing functional groups derived from cellulose-rich cotton fibers, such as hydroxyl, carbonyl and ether groups. Trace amounts of inorganic elements (Si, Ca) are detected, originating from additives, fillers, or residual impurities in garment waste. This elemental profile is characteristic of low-temperature biochars and is consistent with the fibrous morphology observed in SEM (Fig. 2a), as well as with previous reports on textile- and biomass-derived biochars pyrolyzed below 500 °C.[22]

At 600 °C (CGW600, Fig. 2b), the carbon content decreases slightly, accompanied by the appearance of additional heteroatoms such as N, Cl, K, Ca, Ti and Fe in minor quantities. The presence of nitrogen likely originates from residual dyes or finishing agents in textile waste, while inorganic elements are associated with fabric additives and pigment residues. The progressive removal of volatile matter and partial decomposition of oxygenated groups at this temperature results in a more heterogeneous surface chemistry, which correlates well with the fragmented and roughened morphology observed in SEM (Fig. 1b). Such compositional complexity is commonly reported for biochars derived from mixed or treated textile wastes.

For CGW800 (Fig. 2c), a notable increase in oxygen content is observed relative to CGW600, together with measurable nitrogen content and trace inorganic species (Si, S, Cl, Ca). This elemental distribution suggests the formation of stable surface oxygen-containing functional groups, such as carboxyl and phenolic moieties, during high-temperature anaerobic pyrolysis followed by post-pyrolysis exposure. These functional groups play a crucial role in metal ion binding *via* surface complexation and electrostatic interactions, providing a chemical basis for the enhanced adsorption capacity for Pb(II) and Cr(VI) in CGW800. Similar observations have been reported for high-

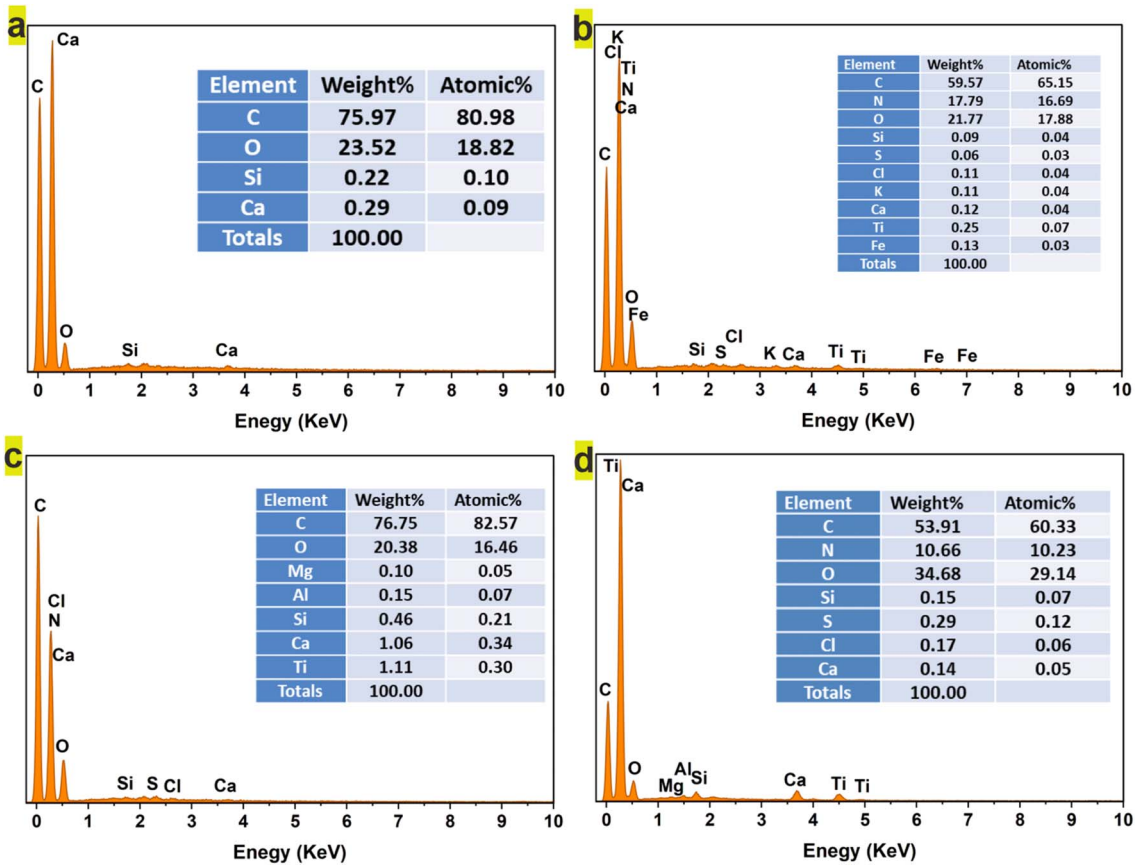


Fig. 2 EDX spectra of CGW at 400 °C (a), 600 °C (b), 800 °C (c) and 900 °C (d).

temperature biochars exhibiting optimal adsorption performance due to a balance between carbonization degree and surface functionality.[27]

At the highest carbonization temperature, 900 °C (CGW900, Fig. 2d), the EDX spectrum shows a pronounced increase in carbon content (>76 wt%) and a corresponding reduction in oxygen content, indicating advanced carbonization and aromatization. Although higher carbon purity is achieved, the depletion of surface heteroatoms and functional groups may reduce the density of chemically active sites available for metal adsorption. In addition, the enrichment of inorganic elements such as Ca and Ti is attributed to the thermal concentration effect resulting from extensive volatilization of organic components.

The inorganic elements identified in the EDX spectra differ between CGWs produced at different temperatures, as expected for real post-industrial garment waste. First, clothing waste typically contains heterogeneous and non-uniformly distributed inorganic-bearing additives (*e.g.*, pigments, fillers, flame retardants, finishing agents, and residual salts), and EDX probes only a near-surface region; therefore, local compositional heterogeneity can lead to different elemental fingerprints between samples. Second, increasing carbonization temperature induces thermal decomposition, volatilization and phase transformation of inorganic-containing compounds. For example, chloride- and sulfur-containing species may partially volatilize or transform into other phases at elevated temperatures, while less volatile metal oxides/mineral residues (*e.g.*, Ca- or Ti-containing phases) may become more prominent. Third, a "thermal concentration" effect occurs because progressive devolatilization removes organic matter and enriches the inorganic fraction at higher temperatures, increasing the probability of detecting certain trace elements. Finally, temperature-driven restructuring (surface cracking, pore evolution, and/or densification) can alter the surface exposure of embedded inorganic particles and thus their detectability by EDX. Collectively, these factors explain why the types and relative intensities of inorganic signals vary among CGW400–CGW900.

Fig. 3 shows the XRD patterns of garment waste-derived biochar (CGW) produced *via* anaerobic pyrolysis at carbonization temperatures of 400, 600, 800 and 900 °C. For CGW400 (Fig. 3a), the XRD pattern is dominated by a broad diffraction band centered at approximately $2\theta = 22–25°$, which can be assigned to the (002) plane of amorphous carbon, along with a weak and diffuse feature around $2\theta \approx 43°$ corresponding to the (100) plane. The broadness and low intensity of these peaks indicate a highly disordered carbon structure with low aromatic stacking, typical of biochars produced at low carbonization temperatures. This result is consistent with incomplete carbonization and the preservation of oxygen-rich functional groups observed in SEM and EDX analyses.

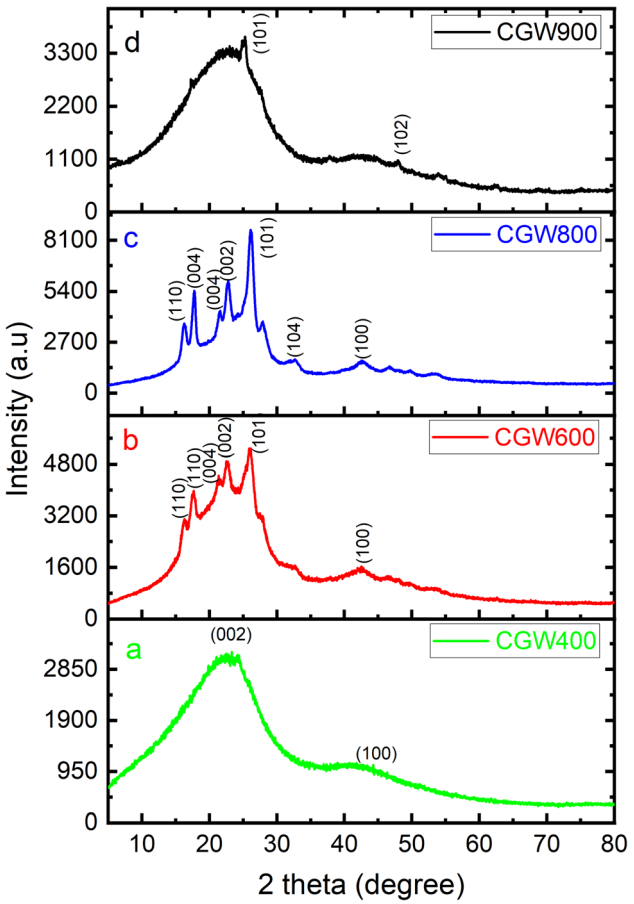


Fig. 3 XRD of CWG at 400 °C (a), 600 °C (b), 800 °C (c) and 900 °C (d).

Upon increasing the carbonization temperature to 600 °C (CGW600, Fig. 3b), the (002) reflection becomes more pronounced and slightly sharper, accompanied by the emergence of weak additional diffraction features. This indicates the onset of aromatic-layer condensation and partial structural ordering, driven by progressive devolatilization and polymer-chain rearrangement during anaerobic pyrolysis. However, the persistence of broad diffraction peaks suggests that the carbon matrix remains predominantly turbostratic and poorly ordered.

At 800 °C (CGW800, Fig. 3c), the XRD pattern exhibits a clearer and more intense (002) peak together with discernible secondary reflections, reflecting a significant increase in short-range structural ordering and aromatic stacking. The narrowing of the (002) peak suggests enhanced alignment of graphene-like layers while retaining a largely disordered framework. This structural configuration is widely regarded as optimal for adsorption applications, as it provides a balance between accessible surface area, pore connectivity, and chemically active sites. The XRD results at 800 °C strongly support the superior Pb(II) and Cr(VI) adsorption performance and enhanced fuel efficiency observed for CGW800.

Further increasing the carbonization temperature to 900 °C (CGW900, Fig. 3d) results in a reduction in peak intensity and a broadening of the diffraction features. Although higher temperatures generally promote increased carbon ordering, excessive thermal treatment can induce structural densification and partial collapse of disordered carbon domains, leading to a decrease in detectable crystallinity. This phenomenon is consistent with SEM observations of denser carbon agglomerates and EDX evidence of reduced surface heteroatom content. Consequently, the marginal improvement in functional performance at 900 °C compared to 800 °C can be attributed to excessive carbon condensation and reduced accessibility of reactive sites.

Fig. 4 presents the FTIR spectra of CGW produced *via* anaerobic pyrolysis at carbonization temperatures ranging from 400 to 900 °C, while the corresponding BET surface area, pore volume, and average pore size are summarized in Table 1. The combined analyses provide direct evidence of the temperature-dependent evolution of surface chemistry and pore structure, which governs the functional performance of CGW.

For CGW400 (Fig. 4a), a broad absorption band centered at approximately 3440 $cm^{-1}$ is clearly observed, corresponding to O–H stretching vibrations of hydroxyl groups originating from cellulose-rich cotton fibers. Additional bands at ~1620 $cm^{-1}$ (C=O stretching of conjugated carbonyl groups), ~1380 $cm^{-1}$ (C–H bending), and ~1040 $cm^{-1}$ (C–O stretching) indicate the presence of abundant oxygen-containing functional groups. This spectral profile is characteristic of incomplete

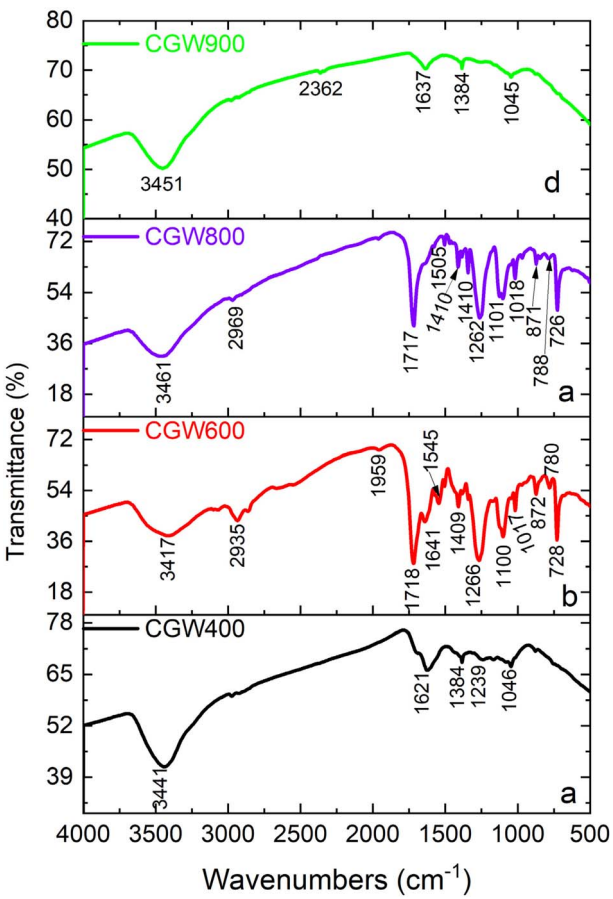


Fig. 4 FTIR analysis of CGW at 400 °C (a), 600 °C (b), 800 °C (c) and 900 °C (d).

Table 1 BET surface area, pore volume and pore size of CGW

| Materials | BET surface area ($m^2\ g^{-1}$) | Pore volume ($cm^3\ g^{-1}$) | Pore size (nm) |
|---|---|---|---|
| CGW400 | 28.53 | 0.024 | 8.69 |
| CGW600 | 56.85 | 0.046 | 3.21 |
| CGW800 | 14.69 | 0.019 | 4.61 |
| CGW900 | 14.65 | 0.010 | 2.65 |

carbonization at low temperature and is commonly reported for textile- and biomass-derived biochars pyrolyzed below 500 °C, where dehydration and devolatilization remain limited.[28,29]

When the carbonization temperature is increased to 600 °C (CGW600, Fig. 4b), the intensity of the O–H stretching band decreases markedly, reflecting progressive dehydration and the removal of labile oxygenated groups during anaerobic pyrolysis. The emergence of absorption bands at ~2935 $cm^{-1}$ (aliphatic C–H stretching) and ~1718 $cm^{-1}$ (C=O stretching) suggests partial transformation of cellulose and polyester components into more condensed carbon structures. Bands in the 1260–1100 $cm^{-1}$ range, attributed to C–O and C–O–C vibrations, indicate the coexistence of residual surface functionalities with an increasingly carbonized matrix. Similar FTIR evolution with increasing pyrolysis temperature has been reported for waste-derived biochars and is associated with enhanced structural condensation and surface heterogeneity. At 800 °C (CGW800, Fig. 4c), the FTIR spectrum shows substantial attenuation of hydroxyl and aliphatic bands, accompanied by more pronounced features in the range of 1500–1400 $cm^{-1}$, which are commonly assigned to aromatic C=C vibrations, as well as persistent bands near ~1717 $cm^{-1}$ related to stable carbonyl groups. The retention of moderate-intensity oxygen-containing functional groups at this temperature indicates the formation of chemically stable surface moieties capable of participating in Pb(II) and Cr(VI) adsorption *via* surface complexation and electrostatic interactions. Previous studies have demonstrated that such balanced surface chemistry is critical for maximizing heavy metal adsorption while maintaining structural stability of biochar.[30,31]

For CGW900 (Fig. 4d), most oxygen-related absorption bands are significantly weakened or nearly absent, indicating advanced carbonization and aromatization. The dominance of weak aromatic-related bands reflects a highly condensed carbon framework with limited surface functional groups. Although this chemical composition is advantageous for fuel applications due to its high carbon purity, the depletion of surface heteroatoms may reduce the density of adsorption-active sites, explaining the lack of a significant improvement in adsorption compared to CGW800.[32,33]

The FTIR observations are strongly supported by the BET results summarized in Table 1. The BET surface area increases from 28.53 $m^2\ g^{-1}$ (CGW400) to 56.85 $m^2\ g^{-1}$ (CGW600), accompanied by an increase in pore volume from 0.024 to 0.046 $m^3\ g^{-1}$, indicating progressive pore development due to volatile release and structural rearrangement at intermediate carbonization temperatures. Concurrently, the average pore size decreases from 8.69 to 3.21 nm, suggesting the formation of smaller mesopores, a feature typical of biochars produced at moderate pyrolysis temperatures. In contrast, further increasing the carbonization temperature to 800 and 900 °C results in a pronounced decrease in BET surface area (14.69 and 14.65 $m^2\ g^{-1}$, respectively) and pore volume, despite increased carbon ordering. This trend is attributed to pore collapse and structural densification induced by excessive thermal severity, as also evidenced by SEM and XRD analyses. Nevertheless, CGW800 retains a moderate average pore size (4.61 nm) and sufficient surface functionality, enabling effective mass transfer and metal ion binding, whereas CGW900, with the smallest pore size (2.65 nm) and lowest pore volume, exhibits reduced accessibility of adsorption-active sites[34,35]

To provide a more intuitive understanding of the textural properties of CGW, the nitrogen adsorption–desorption isotherms and the corresponding pore-size distribution curves are presented in the SI (Fig. S2). All samples exhibit type IV isotherms with hysteresis loops, indicating the presence of mesoporous structures. The pore size distribution further confirms the temperature-dependent evolution of the pore structure, with CGW600 showing a higher contribution of mesopores, consistent with its larger BET surface area and pore volume, as summarized in Table 1.

**Fuel-related characteristics of CGW.** The fuel-related physicochemical characteristics of CGW produced *via* anaerobic pyrolysis at carbonization temperatures of 400, 600, 800, and 900 °C were systematically evaluated through proximate analysis (carbon content, volatile matter, ash and moisture contents), calorific value determination, and visual inspection, as summarized in Fig. 5a–d. The results clearly demonstrate that the carbonization temperature decisively influences the fuel quality and combustion behavior of CGW.

As shown in Fig. 5a, the carbon content of CGW increases markedly from 52.58 wt% at 400 °C to 81.33 wt% at 900 °C, accompanied by a progressive transformation of volatile matter. At a low carbonization temperature (400 °C), incomplete carbonization results in a relatively low carbon fraction and a high volatile content, leading to unstable combustion and excessive release of combustible gases during ignition. Similar behavior has been widely reported for biochars produced from organic and textile wastes at low pyrolysis temperatures, where insufficient devolatilization limits fuel efficiency.[36] In contrast, biochars produced at 800–900 °C exhibit substantially higher carbon content and a more stabilized volatile fraction, promoting more uniform and sustained combustion. This trend is consistent with previous studies on textile waste pyrolysis, where elevated temperatures enhanced carbon enrichment and fuel stability.[37]

The variation in ash and moisture contents with carbonization temperature is illustrated in Fig. 5b. The ash content decreases significantly from 5.67 wt% (400 °C) to 1.67 wt% (900 °C). In comparison, the moisture content declines from 4.28 wt% to 1.07 wt% over the same temperature range. Higher ash content at low temperatures is primarily attributed to residual inorganic additives, dyes, and polyester-derived impurities that are not fully decomposed during mild thermal

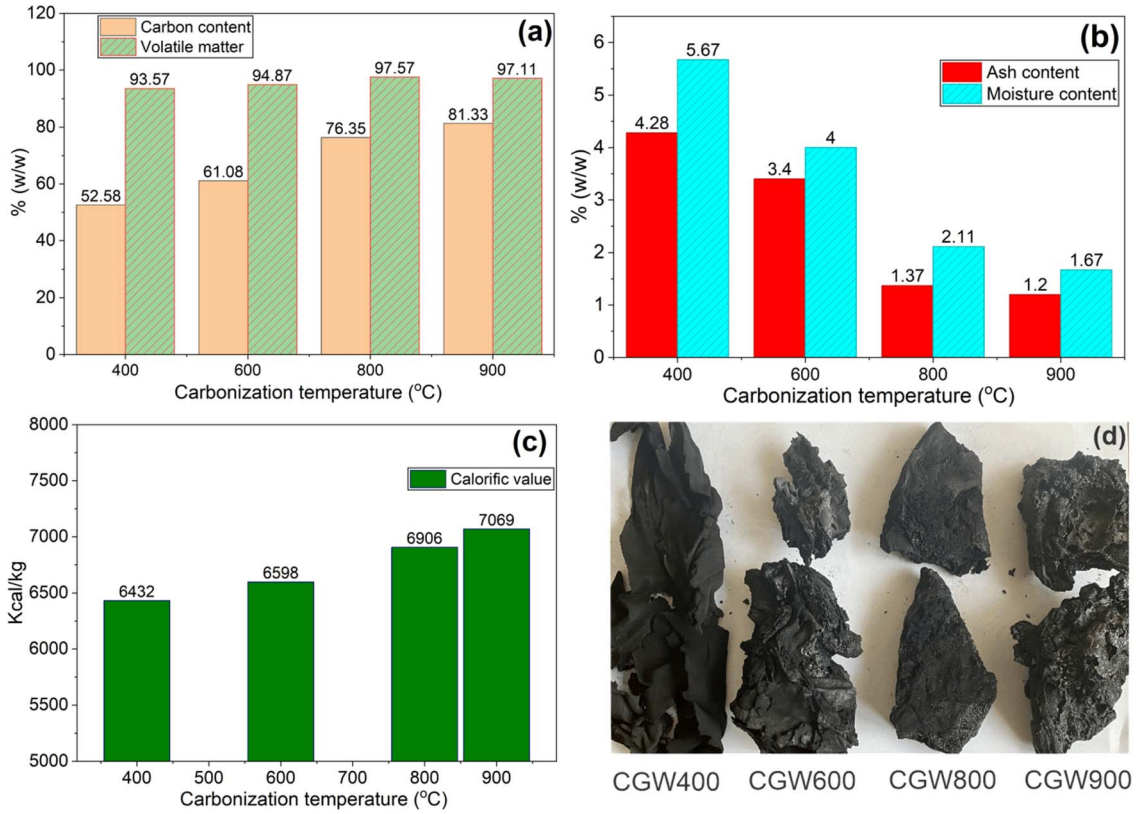


Fig. 5 Characteristics of finished charcoal derived from waste fabric: (a) carbon content and volatile matter, (b) ash and moisture content, (c) calorific value and (d) CGW image.

treatment, as previously observed for textile waste pyrolysis at 300–500 °C.[38] The markedly lower ash and moisture contents obtained at 800–900 °C are favorable for fuel applications, as they reduce non-combustible residues and water-evaporation heat losses, thereby improving combustion efficiency.[39]

The calorific value of CGW, presented in Fig. 5c, increases steadily with carbonization temperature, from 6432 kcal $kg^{-1}$ at 400 °C to 7069 kcal $kg^{-1}$ at 900 °C. The higher heating values obtained at 800–900 °C are directly associated with increased carbon content, reduced ash and moisture fractions, and enhanced aromaticity of the carbon matrix. These values are comparable to, or even exceed, those of commercial honeycomb coal (typically 25–30 MJ $kg^{-1}$), indicating the strong potential of CGW as a solid fuel substitute for domestic and industrial applications. Similar calorific enhancements have been reported for textile waste-derived biochars produced at elevated pyrolysis temperatures.[40]

Visual inspection of the CGW (Fig. 5d) further supports the quantitative analyses. At 400 °C, CGW appears as heterogeneous, brownish-black fragments with poor structural integrity. Increasing the carbonization temperature to 600 °C yields darker, more granular particles, while CGW800 and CGW900 exhibit uniform, glossy black biochars with well-developed porous textures. The improved physical appearance and structural coherence at higher temperatures are consistent with advanced carbonization and pore development, which are known to enhance combustion behavior and heat transfer efficiency.[36]

The results in Fig. 5 indicate that CGW produced at 800–900 °C exhibits optimal fuel-related characteristics, including high carbon content (76.35–81.33 wt%), low ash (1.20–1.37 wt%), minimal moisture (<1.07 wt%) and high calorific value (6906–7069 kcal $kg^{-1}$). These properties ensure efficient and stable combustion while potentially reducing pollutant emissions (*e.g.*, CO and $SO_2$) compared with conventional solid fuels, as reported for biochars derived from organic wastes.[41] Nevertheless, excessive carbonization at 900 °C may induce partial microstructural collapse, compromising mechanical strength without providing substantial additional gains in fuel performance. Consequently, 800 °C can be considered the optimal carbonization temperature, yielding CGW with fuel properties comparable to those of biomass-derived biochars and suitable as a sustainable alternative solid fuel for domestic and industrial combustion systems.

**Fuel performance of CGW.** From the preparation and physicochemical characterization of CGW described earlier, it is evident that this material exhibits promising characteristics for use as a heating fuel. Such an application aligns with waste-to-energy strategies by converting waste residues into useful products, thereby mitigating dependence on fossil fuels. As an initial proof-of-concept evaluation, CGW was therefore tested in water-boiling experiments to determine its viability as a practical fuel under operationally relevant temperatures. The

Table 2 Performance of CGW used as a cooking fuel in a water boiling test

| No. | Type of fuel | Fuel mass (kg) | Water mass (kg) | Boiling time (s) | Total combustion time (s) | Remaining water mass after fuel burnout (kg) | Thermal efficiency (%) | Specific fuel consumption (kg fuel/kg water) |
|---|---|---|---|---|---|---|---|---|
| 1 | CGW400 | 0.5 | 1 | 192 | 2410 | 0.4 | 60 | 0.83 |
| 2 | CGW600 | 0.5 | 1 | 189 | 2582 | 0.36 | 64 | 0.78 |
| 3 | CGW800 | 0.5 | 1 | 186 | 2786 | 0.3 | 70 | 0.71 |
| 4 | CGW900 | 0.5 | 1 | 186 | 2785 | 0.3 | 70 | 0.71 |
| 5 | Coal briquette[a] | 0.5 | 1 | 240 | 1226 | 0.54 | 54 | 0.93 |

[a] Coal briquette refers to a commercial solid fuel manufactured from mined coal powder.

practical applicability of CGW as a household cooking fuel was evaluated through a controlled water-boiling test using CGW produced at different carbonization temperatures (CGW400–CGW900) and compared with a commercial coal briquette. The experimental results are summarized in Table 2, while their interpretation is directly linked to the physicochemical fuel properties discussed in Fig. 5.

As shown in Table 2, the time required to reach the boiling point decreases progressively from 192 s for CGW400 to 186 s for CGW800 and CGW900, whereas the coal briquette requires 240 s under identical conditions. This improvement can be attributed to the combined effects of higher fixed carbon content, lower ash and moisture content, and a more developed porous structure in CGW produced at higher carbonization temperatures. The porous carbon framework enhances oxygen diffusion and heat transfer during combustion, thereby accelerating ignition and heat release, as previously reported for biochars derived from organic and textile wastes.[42,43]

The total combustion duration increases from 2410 s (CGW400) to 2786 s (CGW800) and remains comparable for CGW900 (2785 s), which is significantly longer than that of the coal briquette (1226 s). Prolonged combustion reflects a more stable burning regime, mainly governed by the oxidation of fixed carbon rather than rapid volatilization. The dominant combustion reaction can be simplified as:

$$C_{(s)} + O_2 \rightarrow CO_2 + \text{Heat} \quad (1)$$

At lower carbonization temperatures, residual volatile matter undergoes rapid oxidation:

$$C_xH_y + \left(x + \frac{y}{4}\right)O_2 \rightarrow xCO_2 + \frac{y}{2}H_2O \quad (2)$$

leading to short-lived flames and less efficient heat utilization. In contrast, CGW800 and CGW900, with lower volatile fractions and higher carbon content, exhibit controlled char combustion, which sustains heat release over a more extended period and improves thermal utilization efficiency.[39]

The remaining water mass after complete fuel burnout further confirms the enhanced heat transfer efficiency of high-temperature CGW. While only 0.30 kg of water remains for CGW800 and CGW900, 0.54 kg remains when the coal briquette is used. This indicates that a larger fraction of the released thermal energy is effectively transferred to the water rather than being lost through incomplete combustion or ash accumulation. Such behavior is consistent with the lower ash content (1.20–1.37 wt%) of CGW800–900, which minimizes thermal insulation effects caused by non-combustible residues.

The thermal efficiency ($\eta$) of the cooking process is expressed as:

$$\eta = \frac{m_w c_p (T_b - T_i)}{m_f \times \text{HHV}} \quad (3)$$

where $m_w$ is the water mass (kg), $c_p$ is the specific heat capacity of water (4.18 kJ kg$^{-1}$ K$^{-1}$), $T_b$ and $T_i$ are the boiling and initial temperatures, respectively, $m_f$ is the fuel mass, and HHV is the higher heating value of the fuel.

Based on this evaluation, the thermal efficiency increases from 60–64% for CGW400–600 to 70% for CGW800–900, significantly exceeding that of the coal briquette (54%). Likewise, the specific fuel consumption decreases from 0.83 kg kg$^{-1}$ water (CGW400) to 0.71 kg kg$^{-1}$ water (CGW800–900), compared to 0.93 kg kg$^{-1}$ water for the coal briquette, highlighting the superior fuel utilization efficiency of CGW.[41]

Therefore, CGW800 and CGW900 exhibit optimal cooking fuel performance, characterized by rapid water boiling, prolonged combustion, high thermal efficiency and low fuel consumption, clearly outperforming the coal briquette under identical operating conditions. However, the nearly similar performance of CGW800 and CGW900 suggests that 800 °C is the optimal carbonization temperature, as higher temperatures do not yield significant gains and may induce partial microstructural collapse. These findings confirm that CGW800 is a technically viable and sustainable alternative to conventional coal briquettes for domestic and small-scale industrial cooking applications.

## Adsorption performance of CGW toward Pb(II) and Cr(VI) in aqueous solution

The above experiments confirm that CGW possesses favorable combustion characteristics, making it highly suitable as a fuel when prepared at 800–900 °C. Beyond fuel applications, CGW also offers potential as an adsorbent for environmental pollutants. Therefore, this section evaluates its use as an adsorbent for Pb(II) and Cr(VI) removal, aiming to assess the valorization of cotton gin waste in heavy metal remediation and to determine suitable operational conditions for potential real-world applications.

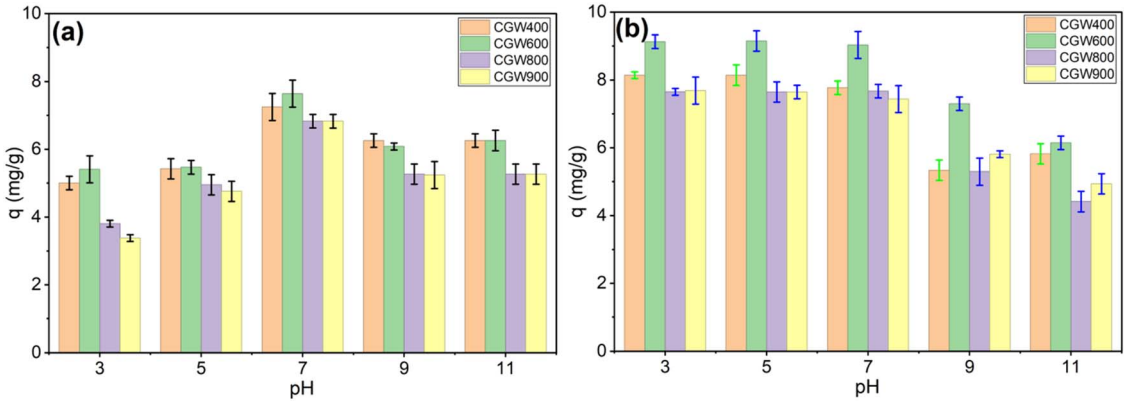


Fig. 6 The influence of the initial pH on Pb (a) and Cr (b) dsorption capacity under the following experimental setup: initial Pb and Cr concentration of 20 mg $L^{-1}$, adsorbent dosage of 0.05 g/20 mL a contact time of 60 min.

**Effect of initial pH on Pb(II) and Cr(VI) adsorption by CGW.** The initial solution pH exerts a critical influence on the adsorption behavior of Pb(II) and Cr(VI) onto CGW, as it directly affects both the surface charge and functional group speciation of CGW and the aqueous speciation of metal ions. As illustrated in Fig. 6, the adsorption capacities of Pb(II) and Cr(VI) vary significantly with pH over the range of 3–11, with CGW600 consistently exhibiting the highest adsorption capacities among all samples, indicating that moderate carbonization provides the most favorable physicochemical conditions for metal uptake.

For Pb(II) adsorption (Fig. 6a), the adsorption capacity increases as the pH increases from 3 to 7 for all CGW samples. At pH 3, Pb(II) uptake is relatively low, with adsorption capacities of 5.00, 5.40, 3.81, and 3.38 mg $g^{-1}$ for CGW400, CGW600, CGW800 and CGW900, respectively. Under these strongly acidic conditions, excess protons ($H^+$) compete with $Pb^{2+}$ ions for surface functional groups, particularly carboxyl and hydroxyl moieties, which remain protonated mainly and thus exhibit limited affinity toward metal cations.[44] As the pH increases toward neutrality, progressive deprotonation of these functional groups occurs:

$$–COOH \Leftrightarrow –COO^- + H^+ \quad (4)$$

$$–OH \Leftrightarrow –O^- + H^+ \quad (5)$$

The formation of negatively charged surface sites enhances Pb(II) adsorption through electrostatic attraction and surface complexation, which can be represented as:

$$2(–COO^-) + Pb^{2+} \rightarrow (–COO)_2Pb \text{ (surface complex)} \quad (6)$$

Consequently, the maximum Pb(II) adsorption capacities are observed at pH 7, reaching 7.64 mg $g^{-1}$ for CGW600, 7.24 mg $g^{-1}$ for CGW400 and 6.82 mg $g^{-1}$ for CGW800 and CGW900. The superior performance of CGW600 at neutral pH can be attributed to its highest BET surface area (56.85 $m^2$ $g^{-1}$) and pore volume (0.046 $cm^3$ $g^{-1}$), which provide a greater number of accessible adsorption sites and facilitate intraparticle diffusion. Although CGW800 and CGW900 possess higher carbonization degrees, their substantially lower surface areas limit the availability of adsorption-active sites. At alkaline pH (9–11), Pb(II) adsorption capacities decrease slightly (*e.g.*, 6.07–6.25 mg $g^{-1}$ for CGW600), which can be partly attributed to the formation of hydroxo species and precipitation reactions such as:

$$Pb^{2+} + 2OH^- \rightarrow Pb(OH)_2(s) \quad (7)$$

Hereby reducing the contribution of true surface adsorption.[45]

In contrast, the adsorption behavior of Cr(VI) (Fig. 6b) exhibits a reverse pH dependence due to the anionic nature of Cr(VI) species in aqueous solution. At pH 3, Cr(VI) adsorption capacities are relatively high, reaching 9.12 mg $g^{-1}$ for CGW600, compared with 8.14 mg $g^{-1}$ for CGW400, 7.65 mg $g^{-1}$ for CGW800, and 7.69 mg $g^{-1}$ for CGW900. Under acidic conditions, Cr(VI) predominantly exists as $HCrO_4^-$ and $Cr_2O_7^{2-}$,[46] while protonation of CGW surface hydroxyl groups generates positively charged sites according to:

$$HCrO_4^- + 7H^+ + 3e^- \rightarrow Cr^{3+} + 4H_2O \quad (8)$$

followed by immobilization of Cr(III) *via* surface complexation or precipitation:

$$Cr^{3+} + 3OH^- \rightarrow Cr(OH)_3(s) \quad (9)$$

Although chromium speciation was not directly analyzed in this study, the pronounced pH dependence and higher adsorption capacities under acidic conditions are consistent with the widely reported mechanism for biochar-based adsorbents. At higher pH, increased deprotonation makes the surface more negative and intensifies electrostatic repulsion toward chromate anions, while $OH^-$ competes for surface sites – together leading to the observed decline in Cr(VI) uptake at pH 9–11.[45,47]

Overall, the results clearly demonstrate that CGW600 exhibits the highest adsorption capacities for both Pb(II) and Cr(VI) across the investigated pH range, achieving peak values of

7.64 mg $g^{-1}$ for Pb(II) at pH 7 and 9.14 mg $g^{-1}$ for Cr(VI) at pH 5. This superior performance arises from the synergistic combination of abundant surface functional groups and the highest accessible surface area and pore volume among the CGW samples. While CGW800 may be optimal for fuel applications due to its higher carbon content and calorific value, CGW600 is the optimal material for adsorption-based water treatment, underscoring the importance of tailoring the carbonization temperature to specific end-use applications in the valorization of textile waste.

**Pb and Cr adsorption kinetics and isotherms.** The adsorption kinetics of Pb(II) and Cr(VI) onto garment waste-derived biochar (CGW) were investigated to elucidate the rate-controlling mechanisms and to differentiate further the adsorption performance of CGW produced at different carbonization temperatures. The experimental kinetic data (Fig. 7) were fitted using the pseudo-first-order (PFO), pseudo-second-order (PSO), and Elovich models, and the corresponding kinetic parameters are summarized in Table 3.

As shown in Fig. 7, the adsorption of both Pb(II) and Cr(VI) on all CGW samples exhibits a characteristic two-stage kinetic behavior, consisting of a rapid uptake during the initial 20–30 min followed by a slower approach to equilibrium, which is typically reached after approximately 90–120 min. The initial fast stage is attributed to the abundant availability of external surface sites and strong driving forces arising from high concentration gradients, whereas the subsequent slower stage is governed by diffusion into internal pores and the progressive occupation of less accessible sites. Such kinetic features are widely reported for biochar-based adsorbents and indicate a combined contribution from surface adsorption and intra-particle diffusion.[48]

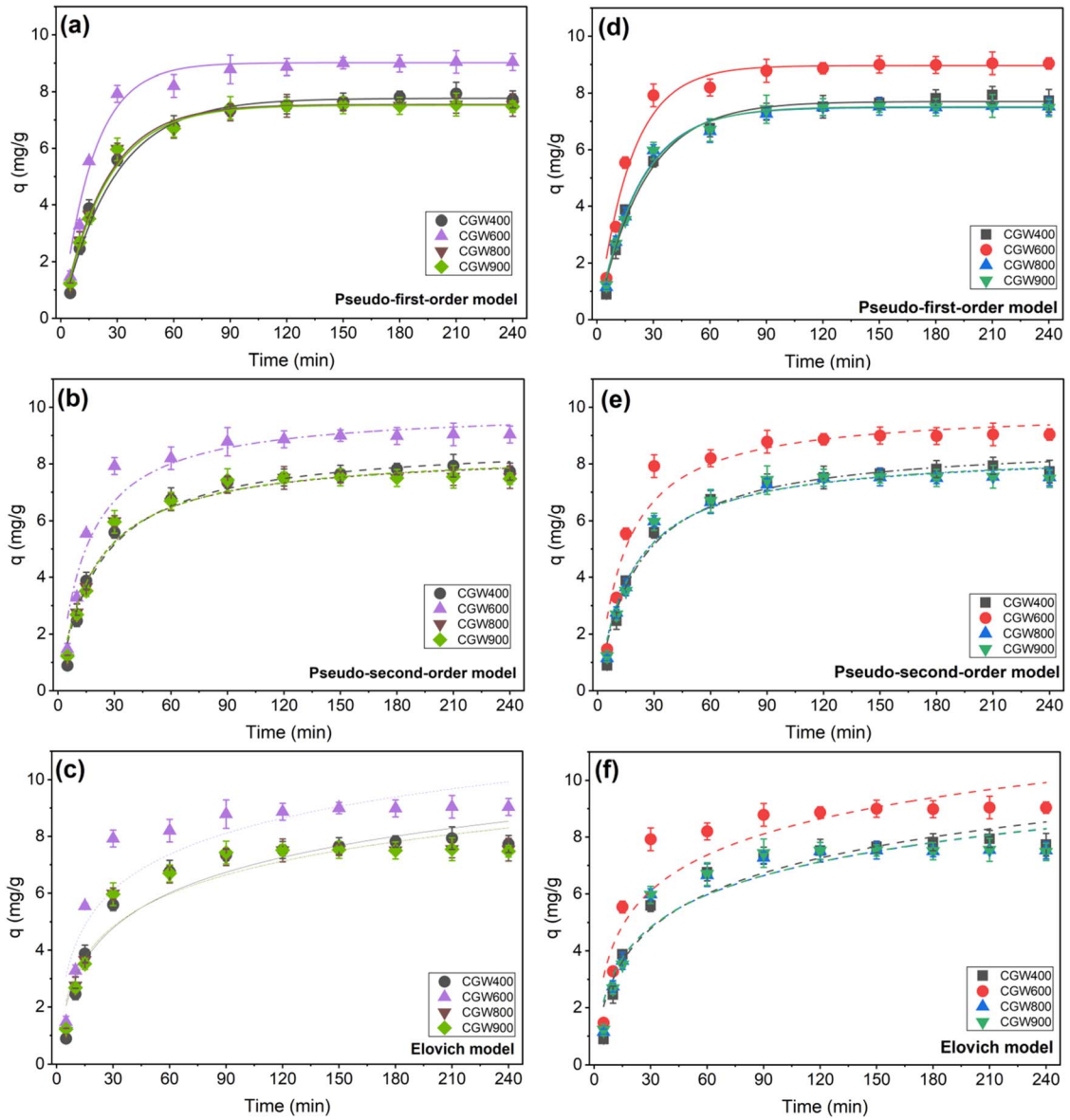


Fig. 7 Kinetic analysis of Pb (a–c) and Cr (d–f) removal by CGW.

Table 3 Kinetic model parameters for Pb and Cr adsorption using CGW

| | CGW400 | | CGW600 | | CGW800 | | CGW900 | |
|---|---|---|---|---|---|---|---|---|
| | Pb | Cr | Pb | Cr | Pb | Cr | Pb | Cr |
| **Pseudo-first-order model** | | | | | | | | |
| $q_e$ (mg g$^{-1}$) | 7.76 ± 0.19 | 7.70 ± 0.11 | 9.01 ± 0.25 | 8.96 ± 0.16 | 7.54 ± 0.16 | 7.49 ± 0.09 | 7.52 ± 0.10 | 7.51 ± 0.08 |
| $k_1$ | 0.0363 ± 0.0031 | 0.0404 ± 0.0025 | 0.0588 ± 0.0042 | 0.0555 ± 0.0047 | 0.0432 ± 0.002 | 0.0453 ± 0.0024 | 0.0420 ± 0.0016 | 0.0444 ± 0.002 |
| $R^2$ | 0.9886 | 0.98954 | 0.9703 | 0.9765 | 0.9905 | 0.9917 | 0.9962 | 0.9931 |
| **Pseudo-second-order model** | | | | | | | | |
| $q_{m,cal}$ (mg g$^{-1}$) | 8.79 ± 0.25 | 8.79 ± 0.25 | 9.94 ± 0.37 | 9.95 ± 0.37 | 8.44 ± 0.24 | 8.44 ± 0.24 | 8.47 ± 0.25 | 8.47 ± 0.26 |
| $k_2$ | 0.0053 ± 0.0008 | 0.0053 ± 0.00008 | 0.0069 ± 0.0014 | 0.0069 ± 0.0014 | 0.0065 ± 0.0010 | 0.0065 ± 0.001 | 0.0063 ± 0.0010 | 0.0063 ± 0.00105 |
| $R^2$ | 0.9794 | 0.9795 | 0.9463 | 0.9464 | 0.9743 | 0.9743 | 0.9721 | 0.9721 |
| **Elovich model** | | | | | | | | |
| $a$ | 0.743 ± 0.26 | 0.744 ± 0.262 | 1.571 ± 0.864 | 1.571 ± 0.864 | 0.916 ± 0.373 | 0.916 ± 0.373 | 0.901 ± 0.375 | 0.9008 ± 0.375 |
| $b$ | 0.535 ± 0.069 | 0.535 ± 0.069 | 0.535 ± 0.089 | 0.535 ± 0.089 | 0.587 ± 0.081 | 0.588 ± 0.081 | 0.583 ± 0.082 | 0.584 ± 0.082 |
| $R^2$ | 0.9315 | 0.9315 | 0.8628 | 0.8628 | 0.9136 | 0.9136 | 0.9094 | 0.9094 |
| $q_{e,exp}$ (mg g$^{-1}$) | 8.34 ± 0.23 | 7.34 ± 0.31 | 9.43 ± 0.26 | 8.78 ± 0.18 | 7.84 ± 0.21 | 7.27 ± 0.11 | 7.81 ± 0.13 | 7.43 ± 0.12 |

For Pb(II) adsorption, the experimentally determined equilibrium adsorption capacities ($q_{e,exp}$) follow the order CGW600 (9.43 ± 0.26 mg g$^{-1}$) > CGW400 (8.34 ± 0.23 mg g$^{-1}$) > CGW800 (7.84 ± 0.21 mg g$^{-1}$) ≈ CGW900 (7.81 ± 0.13 mg g$^{-1}$). This trend is consistent with the adsorption profiles shown in Fig. 7a–c and confirms that CGW600 achieves the highest Pb(II) uptake. Among the kinetic models, the pseudo-first-order model provides an excellent fit, with high coefficients of determination ($R^2$ = 0.9703–0.9962). In particular, CGW600 exhibits a relatively high PFO rate constant ($k_1$ = 0.0588 ± 0.0042 min$^{-1}$), indicating faster Pb(II) uptake than the other samples. Moreover, the PFO-calculated equilibrium capacity for CGW600 ($q_e$ = 9.01 ± 0.25 mg g$^{-1}$) is in close agreement with the experimental value, suggesting that Pb(II) adsorption is primarily governed by surface-site occupation and concentration-gradient-driven mass transfer, rather than being strictly limited by chemical reaction kinetics.[49]

Although the pseudo-second-order model yields higher calculated adsorption capacities ($q_{m,cal}$ = 9.94 ± 0.37 mg g$^{-1}$ for CGW600), its lower $R^2$ values (0.9463–0.9795) and the noticeable deviation between calculated and experimental capacities indicate that PSO slightly overestimates the adsorption capacity. This implies that while surface interactions contribute to Pb(II) uptake, chemisorption is not the sole rate-limiting step. The Elovich model, typically associated with adsorption on energetically heterogeneous surfaces, shows the lowest $R^2$ values (0.8628–0.9315), suggesting that Pb(II) adsorption on CGW is better described by a relatively uniform distribution of accessible sites,[50] particularly for CGW600.

A similar kinetic behavior is observed for Cr(VI) adsorption (Fig. 7d–f). The experimental equilibrium capacities follow the order CGW600 (8.78 ± 0.18 mg g$^{-1}$) > CGW400 (7.34 ± 0.31 mg g$^{-1}$) > CGW900 (7.43 ± 0.12 mg g$^{-1}$) ≈ CGW800 (7.27 ± 0.11 mg g$^{-1}$) (Table 3), again demonstrating the superior performance of CGW600. The PFO model provides the best overall description of Cr(VI) adsorption kinetics, with high $R^2$ values (0.9765–0.9931) and PFO-calculated capacities for CGW600 ($q_e$ = 8.96 ± 0.16 mg g$^{-1}$) that closely agree with the experimental data. The relatively high rate constant for CGW600 ($k_1$ = 0.0555 ± 0.0047 min$^{-1}$) reflects rapid initial Cr(VI) uptake, which is consistent with strong electrostatic attraction between protonated CGW surfaces and anionic chromate species under the selected experimental conditions.[16]

The PSO model yields higher calculated capacities for Cr(VI) (up to 9.95 ± 0.379.95 mg g$^{-1}$ for CGW600), but again shows lower goodness-of-fit than the PFO model. This suggests that, although surface reactions and possible redox interactions may occur, the overall Cr(VI) adsorption kinetics are primarily governed by external mass transfer and surface-site accessibility rather than by a single chemisorption-controlled step. The Elovich parameters further indicate surface heterogeneity, with CGW600 exhibiting the highest initial adsorption rate constant ($\alpha$ = 1.571 ± 0.864 mg g$^{-1}$ min$^{-1}$), reflecting the abundance of readily accessible active sites on this material.

The systematic overestimation of $q_e$ by PSO model does not necessarily indicate that chemisorption is the rate-limiting step. PSO fitting is highly sensitive to data points at late stages of adsorption and to experimental uncertainty near equilibrium; thus, deviations in $q_{e,cal}$ may arise from model-structure limitations and linearization effects rather than reflecting a dominant chemisorption-controlled pathway. In the present system, the superior fit of the PFO model (higher $R^2$ and closer agreement between $q_{e,cal}$ and $q_{e,exp}$) suggests that adsorption kinetics are primarily governed by surface-site accessibility and mass-transfer processes (film/intraparticle diffusion), consistent with the observed two-stage uptake behavior. Nevertheless, chemical interactions (*e.g.*, surface complexation/ion exchange for Pb(II) and reduction-assisted immobilization for Cr(VI)) may

 

still contribute as supporting processes, particularly in the later stage as the system approaches equilibrium. Still, they are unlikely to be the sole rate-controlling step.

The consistently superior kinetic performance of CGW600 for both Pb(II) and Cr(VI) can be directly linked to its textural and chemical properties. CGW600 possesses the highest BET surface area and pore volume among all samples, facilitating rapid diffusion of metal ions to adsorption sites, while still retaining a sufficient density of oxygen-containing functional groups to promote electrostatic attraction, surface complexation, and, in the case of Cr(VI), potential reduction-assisted immobilization.[51] In contrast, CGW800 and CGW900, despite higher carbonization degrees, exhibit reduced surface areas due to pore densification at elevated temperatures, thereby limiting both adsorption rates and equilibrium capacities.

From an integrated perspective, the combined kinetic modeling and experimental results demonstrate that Pb(II) and Cr(VI) adsorption on CGW is best described by the pseudo-first-order model, indicating that surface accessibility and mass transfer dominate the adsorption process. Among the investigated materials, CGW600 emerges as the optimal adsorbent, achieving the highest experimental capacities and the fastest adsorption rates for both contaminants. These findings further support selecting CGW600 for subsequent adsorption isotherm and thermodynamic analyses, while reinforcing the conclusion that a moderate carbonization temperature is critical for maximizing adsorption performance in textile waste-derived biochars.

**Adsorption isotherms.** The equilibrium adsorption behavior of Pb(II) and Cr(VI) onto CGW was investigated using Langmuir,

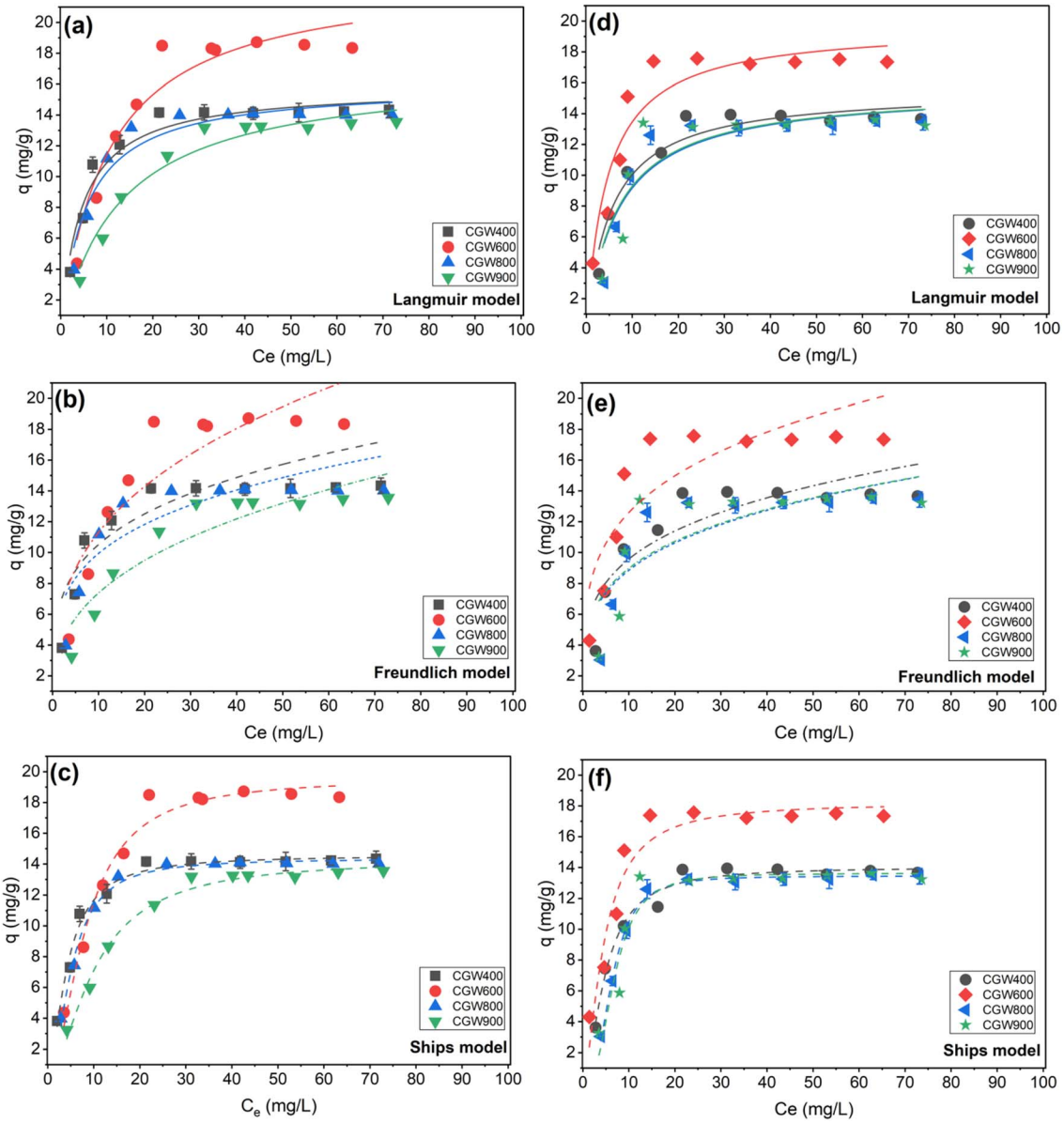


Fig. 8 Isotherm model for Pb (a–c) and Cr (d–f) adsorption using CGW.

Table 4 Parameters and correlation coefficients of Pb and Cr adsorption isotherm models with CGW

| | CGW400 | | CGW600 | | CGW800 | | CGW900 | |
|---|---|---|---|---|---|---|---|---|
| | Pb | Cr | Pb | Cr | Pb | Cr | Pb | Cr |
| **Langmuir model** | | | | | | | | |
| $q_{max}$ (mg g$^{-1}$) | 15.80 ± 0.52 | 15.53 ± 0.62 | 23.18 ± 1.48 | 19.68 ± 1.08 | 15.96 ± 0.64 | 15.60 ± 1.06 | 16.93 ± 0.87 | 15.59 ± 1.34 |
| $K_L$ (L mg$^{-1}$) | 0.221 ± 0.036 | 0.183 ± 0.034 | 0.097 ± 0.022 | 0.216 ± 0.052 | 0.181 ± 0.035 | 0.143 ± 0.041 | 0.075 ± 0.013 | 0.147 ± 0.054 |
| $R^2$ | 0.9531 | 0.9393 | 0.9326 | 0.9073 | 0.9344 | 0.8644 | 0.9597 | 0.7941 |
| **Freundlich model** | | | | | | | | |
| $K_F$ ((mg g$^{-1}$)/(mg L$^{-1}$)$^n$) | 5.912 ± 1.178 | 5.387 ± 1.069 | 5.199 ± 1.301 | 7.083 ± 1.458 | 5.588 ± 1.166 | 4.847 ± 1.253 | 3.219 ± 0.775 | 4.991 ± 1.437 |
| $n_F$ | 4 ± 0.89 | 4 ± 0.892 | 2.963 ± 0.628 | 4 ± 0.966 | 4 ± 0.935 | 3.819 ± 1.053 | 2.773 ± 0.499 | 3.917 ± 1.238 |
| $R^2$ | 0.7131 | 0.7652 | 0.8066 | 0.7375 | 0.7409 | 0.6955 | 0.8601 | 0.6343 |
| **Ships model** | | | | | | | | |
| $q_m$ | 14.56 ± 0.29 | 14.03 ± 0.35 | 19.56 ± 0.73 | 18.19 ± 0.93 | 14.35 ± 0.18 | 13.44 ± 0.12 | 14.30 ± 0.45 | 13.61 ± 0.59 |
| $b$ | 0.099 ± 0.027 | 0.067 ± 0.024 | 0.023 ± 0.012 | 0.088 ± 0.058 | 0.047 ± 0.011 | 0.0056 ± 0.0018 | 0.021 ± 0.009 | 0.0048 ± 0.008 |
| $n$ | 0.621 ± 0.070 | 0.585 ± 0.081 | 0.555 ± 0.081 | 0.626 ± 0.158 | 0.533 ± 0.041 | 0.359 ± 0.022 | 0.601 ± 0.069 | 0.361 ± 0.107 |
| $R^2$ | 0.9849 | 0.9787 | 0.9763 | 0.9327 | 0.9924 | 0.9954 | 0.9876 | 0.9036 |

Freundlich, and Sips isotherm models, as illustrated in Fig. 8 with the corresponding fitted parameters summarized in Table 4. For all CGW samples, the adsorption capacity increases rapidly at low equilibrium concentrations ($C_e$). It gradually approaches a plateau at higher $C_e$, indicating progressive occupation of available adsorption sites followed by saturation. This characteristic trend suggests adsorption on a finite number of active sites, a feature typical of biochar-based sorbents.[52]

Across all CGW samples and for both metals, the Sips model provides the best overall fit, with consistently high coefficients of determination (Pb: $R^2$ = 0.9763–0.9924; Cr: $R^2$ = 0.9036–0.9954). By contrast, the Langmuir fits are moderate (Pb: $R^2$ = 0.9326–0.9597; Cr: $R^2$ = 0.7941–0.9393), while the Freundlich fits are relatively poor (Pb: $R^2$ = 0.7131–0.8601; Cr: $R^2$ = 0.6343–0.7652). The clear superiority of Sips strongly suggests that adsorption occurs on energetically heterogeneous surfaces but still exhibits finite-site saturation at higher concentrations – precisely the mixed behavior Sips is designed to capture (Langmuir-like at high $C_e$, Freundlich-like at low $C_e$). This interpretation aligns well with the biochar literature, where Sips models frequently outperform Langmuir/Freundlich models for metal ions due to heterogeneous surface functional groups and mineral phases.[53]

For Pb(II), the maximum adsorption capacity derived from the Langmuir model ($q_{max}$) is markedly higher for CGW600 (23.18 ± 1.48 mg g$^{-1}$) than for CGW400 (15.80 ± 0.52 mg g$^{-1}$), CGW800 (15.96 ± 0.64 mg g$^{-1}$), and CGW900 (16.93 ± 0.87 mg g$^{-1}$). Consistently, the Sips capacity parameter $q_m$ also identifies CGW600 as the best performer (19.56 ± 0.73 mg g$^{-1}$), while the remaining samples are clustered around 14.30–14.56 mg g$^{-1}$. This ranking mirrors the kinetic outcomes (Table 3) where CGW600 achieved the highest $q_{e,exp}$ for Pb(II), and it is mechanistically coherent with the textural/chemical advantages of CGW600 (highest BET surface area and pore volume while retaining sufficient oxygenated groups). Such "moderate-temperature" biochars commonly maximize adsorption because they balance (i) accessibility of pores/surface area with (ii) retention of complexation-capable functional groups, whereas harsher carbonization can reduce functional group density and/or accessibility *via* pore rearrangement.[52]

The Langmuir affinity constant $K_L$ for Pb(II) is lower for CGW600 (0.097 ± 0.022 L mg$^{-1}$) than for CGW400 (0.221 ± 0.036 L mg$^{-1}$) and CGW800 (0.181 ± 0.035 L mg$^{-1}$), indicating that CGW600 achieves its superior capacity primarily through a larger population of effective adsorption sites rather than uniformly stronger affinity. This is a common signature of heterogeneous adsorbents: high-capacity materials may exhibit broader distributions of site energies, with strong binding on some sites and weaker binding on others, yielding high overall uptake but moderate average affinity in a single-parameter Langmuir description. The Sips heterogeneity parameter $n$ further supports this view, with $n < 1$ for Pb(II) across all samples (*e.g.*, CGW600: 0.555 ± 0.081), indicating heterogeneous adsorption energies rather than ideal monolayer uniformity.[53]

A similar trend is observed for Cr(VI) adsorption. For Cr(VI), the same central conclusion holds: CGW600 exhibits the highest equilibrium capacity among all samples. Langmuir $q_{max}$ values follow CGW600 (19.68 ± 1.08 mg g$^{-1}$) > CGW400 (15.53 ± 0.62 mg g$^{-1}$) ≈ CGW900 (15.59 ± 1.34 mg g$^{-1}$) ≈ CGW800 (15.60 ± 1.06 mg g$^{-1}$), while the Sips $q_m$ values show CGW600 (18.19 ± 0.93 mg g$^{-1}$) substantially exceeding the others (13.44–14.03 mg g$^{-1}$). Importantly, for Cr(VI) the Langmuir affinity constant $K_L$ is relatively high for CGW600 (0.216 ± 0.052 L mg$^{-1}$), implying that CGW600 provides not only more adsorption sites but also favorable interactions with chromate species under the tested conditions.[54] Mechanistically, Cr(VI) removal on biochar often involves a coupled adsorption–reduction–immobilization pathway, in which anionic chromate is first adsorbed and then partially reduced to Cr(III), which is

 

subsequently stabilized on the surface *via* complexation/precipitation. This multi-step nature inherently generates heterogeneity in apparent adsorption energies and is consistent with Sips-type behavior. Prior mechanistic work has shown that biochar's inorganic fraction and surface functionalities can participate in Cr(VI) reduction and subsequent formation of Cr(III) species (*e.g.*, hydroxides/oxides). At the same time, Langmuir-type saturation may still emerge at high concentrations due to limited reactive/adsorptive sites.[54] The Sips heterogeneity parameter nnn for Cr(VI) further indicates more substantial heterogeneity for high-temperature samples (*e.g.*, CGW800: 0.359 ± 0.022; CGW900: 0.361 ± 0.107) compared with CGW600 (0.626 ± 0.158), suggesting that while CGW800/900 may retain subsets of strong sites, their overall accessible site population is smaller (consistent with their lower $q_m$). Conversely, CGW600 combines higher capacity with a more favorable overall site distribution, consistent with its superior performance observed in both pH and kinetic results.

The fitted isotherm behavior observed here – Sips > Langmuir > Freundlich – is consistent with many reports on heavy-metal adsorption by biochars, where surface heterogeneity (multiple functional groups, mineral phases, and pore hierarchies) makes two-parameter models insufficient, while Sips captures both heterogeneity and saturation. In particular, the finding that a moderate carbonization temperature (600 °C) maximizes adsorption capacity aligns closely with the broader biochar literature summarized in recent reviews, which emphasize that adsorption performance depends on a balance between surface chemistry and accessible porosity rather than carbon content alone. Taken together with the kinetic analysis (Fig. 7 and Table 3), the isotherm results confirm that CGW600 is the optimal adsorbent among the investigated CGW materials, achieving the highest capacities for both Pb(II) and Cr(VI) and exhibiting equilibrium behavior best captured by the Sips model – consistent with adsorption on heterogeneous surfaces with finite saturation.

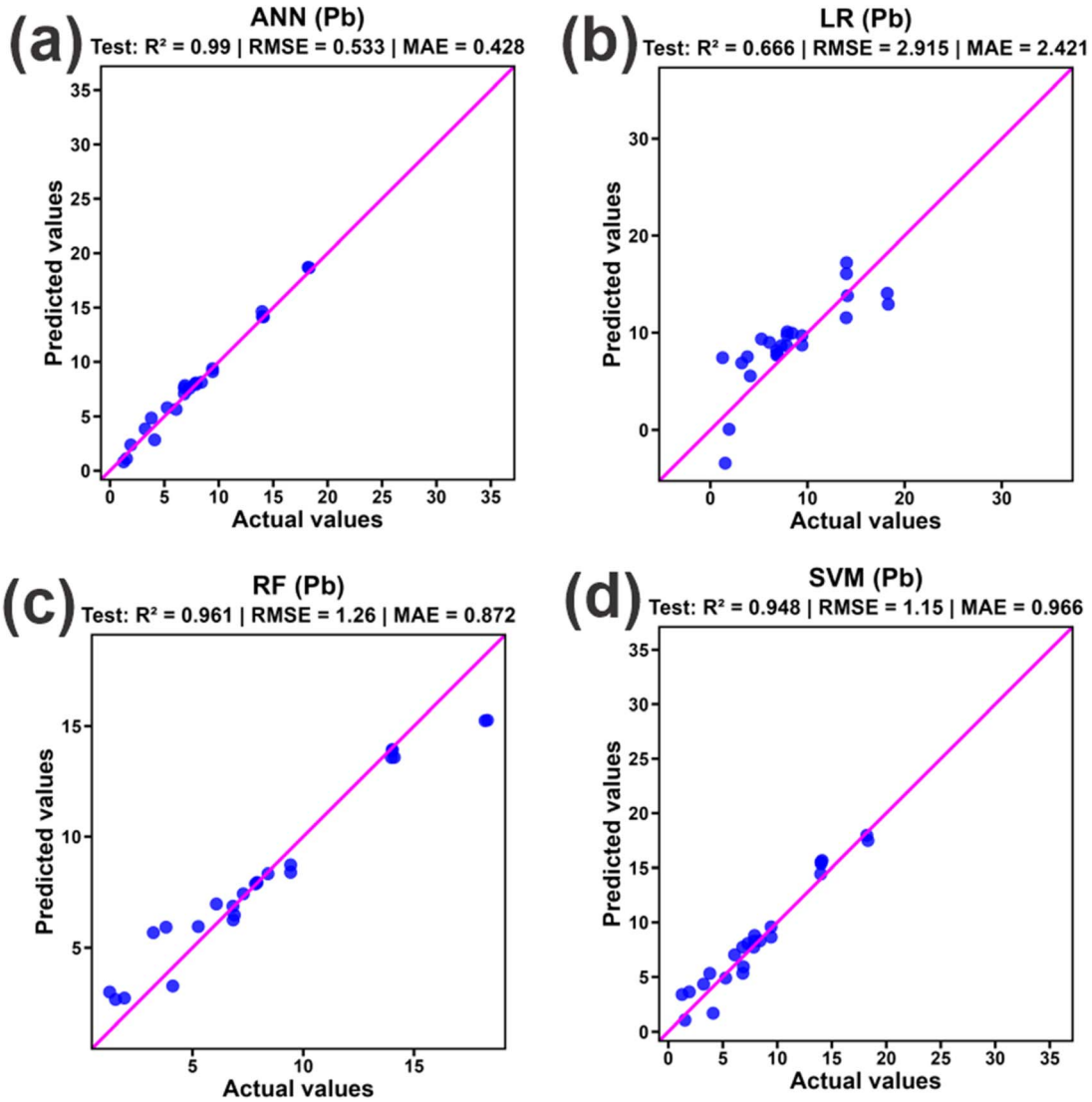


Fig. 9 The prediction of ML models: ANN (a); LR (b); RF (c); SVM (d) for Pb adsorption capacity by CGW.

**Machine learning model for Pb and Cr adsorption capacity prediction.** The predictive capabilities of four distinct machine learning algorithms – ANN, LR, RF and SVM – were rigorously evaluated to estimate the adsorption capacity of Pb(II) and Cr(VI) onto the CGW adsorbent. Model performance was quantified using $R^2$, RMSE, and MAE.

For predicting Pb(II) adsorption capacity, the ANN model demonstrated superior performance compared to the other algorithms. As illustrated in Fig. 9, the ANN model achieved the highest accuracy ($R^2 = 0.99$) and the lowest error rates (RMSE = 0.533, MAE = 0.428). This aligns with previous studies which have consistently shown that ANN architectures are highly effective in modeling the non-linear behavior of heavy metal adsorption processes.[55] The RF and SVM models also demonstrated strong predictive performance, with $R^2$ values of 0.961 and 0.948, respectively. In sharp contrast, the LR model failed to capture the data's complexity, yielding an $R^2$ of 0.666 and an RMSE of 2.915.

A similar trend was observed for the prediction of Cr(VI) adsorption capacity (Fig. 10). The ANN algorithm again proved to be the most reliable model, attaining an $R^2$ of 0.987 and an RMSE of 0.558. The hierarchy of model accuracy for Cr(VI) followed the order: ANN > RF ($R^2 = 0.956$) > SVM ($R^2 = 0.936$) > LR ($R^2 = 0.691$). These findings are consistent with the comparative analyses by Salazar-Rojas *et al.* (2022)[56] and Parveen *et al.* (2017),[57] who reported that ensemble methods (such as RF) and non-linear models (such as SVM and ANN) significantly outperform linear regression in predicting adsorption efficiencies due to the complex, multivariate nature of solid–liquid interface interactions.

The visual distribution of predicted *versus* actual values reinforces these statistical findings. In the scatter plots for ANN, RF and SVM, the data points are tightly clustered around the bisector line (1 : 1 line), indicating a high degree of precision. Conversely, the LR model displays a wide dispersion of data points away from the diagonal. This suggests that the adsorption process involves complex, non-linear interactions that

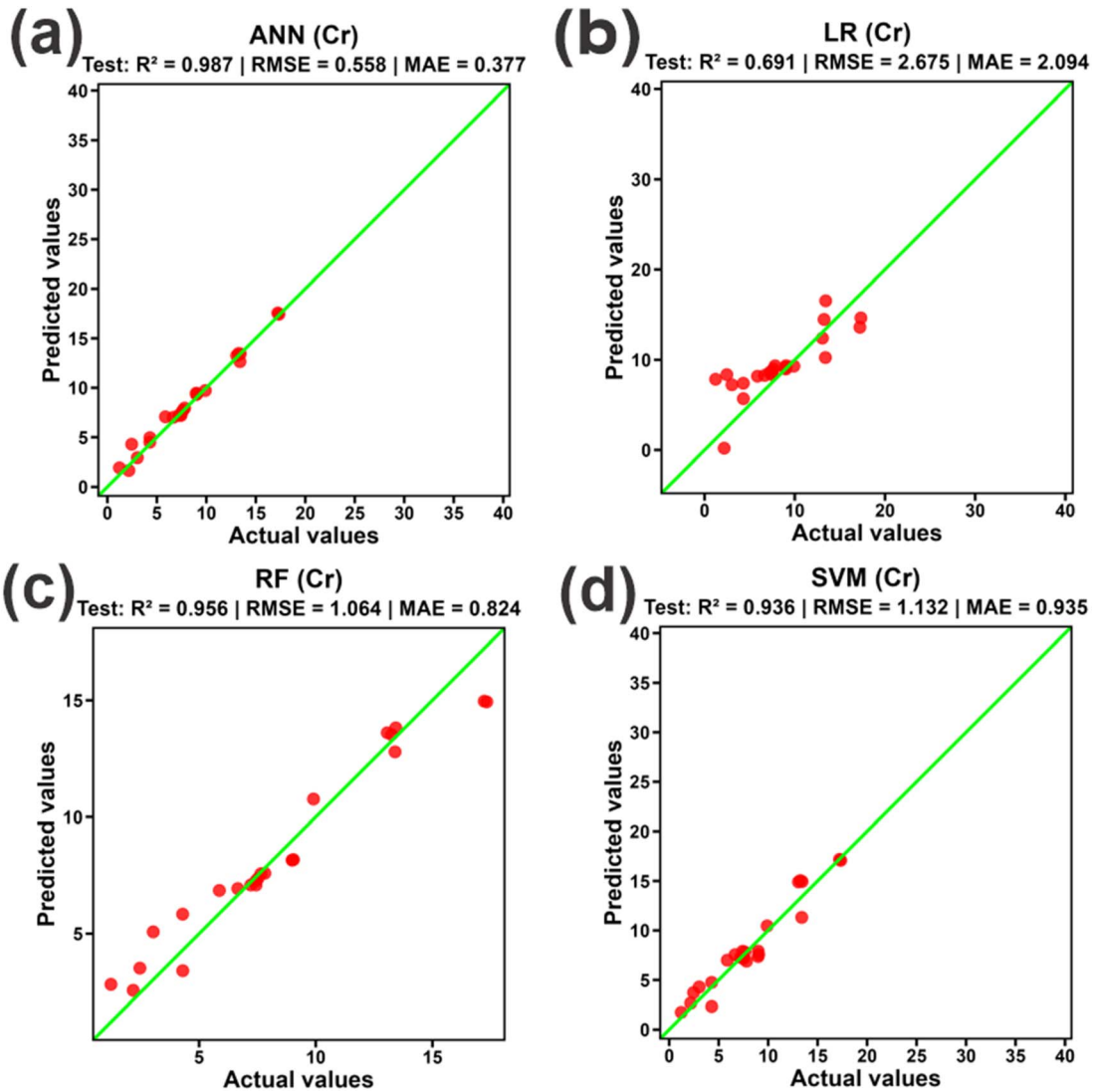


Fig. 10 The prediction of ML models: ANN (a); LR (b); RF (c); SVM (d) for Cr adsorption capacity by CGW.

linear algorithms cannot adequately model. In contrast, non-linear models, such as ANNs, are well-suited to capture the intricate topology of adsorption isotherms and kinetics.

To elucidate the influence of specific experimental parameters on the adsorption efficiency, a feature importance analysis was conducted. This analysis identifies which input variables – initial concentration (Pb_con/Cr_con), adsorbent dosage (Ads_dos), time, temperature (Temp.), and pH – most significantly affect the model outputs.

For Pb(II) (Fig. 11), initial metal concentration (Pb_con) emerged as the most influential factor across all models (importance scores > 0.85 in RF and SVM), followed by adsorbent dosage (Ads_dos, ~0.70) and pH (~0.55). At the same time, contact time and temperature contributed less (<0.40). This hierarchy reflects the dominance of mass transfer in Pb(II) uptake, where higher concentrations drive steeper gradients and dosage modulates site availability, consistent with Langmuir-type saturation observed in isotherm studies.[58] For Cr(VI) (Fig. 12), pH ranked highest (~0.80), underscoring its role in speciation and electrostatic interactions, with initial concentration and dosage following closely (~0.65–0.75), aligning with the pH-dependent reduction–adsorption pathway.[59] The consistency in importance rankings across models enhances interpretability, with RF providing the most robust feature selection due to its ensemble-based permutation importance.

The superior performance of RF and SVM over ANN and LR highlights the efficacy of non-parametric approaches in handling the inherent complexities of biochar adsorption systems, such as surface heterogeneity and variable interactions, as corroborated by prior studies on heavy metal remediation.[60–62] The models' high $R^2$ values surpass those reported in similar ML applications for biochar-based adsorbents (*e.g.*, $R^2$ ~0.90), attributable to the comprehensive dataset and tailored preprocessing. Furthermore, the variable importance insights offer mechanistic validation: for Pb(II), concentration-

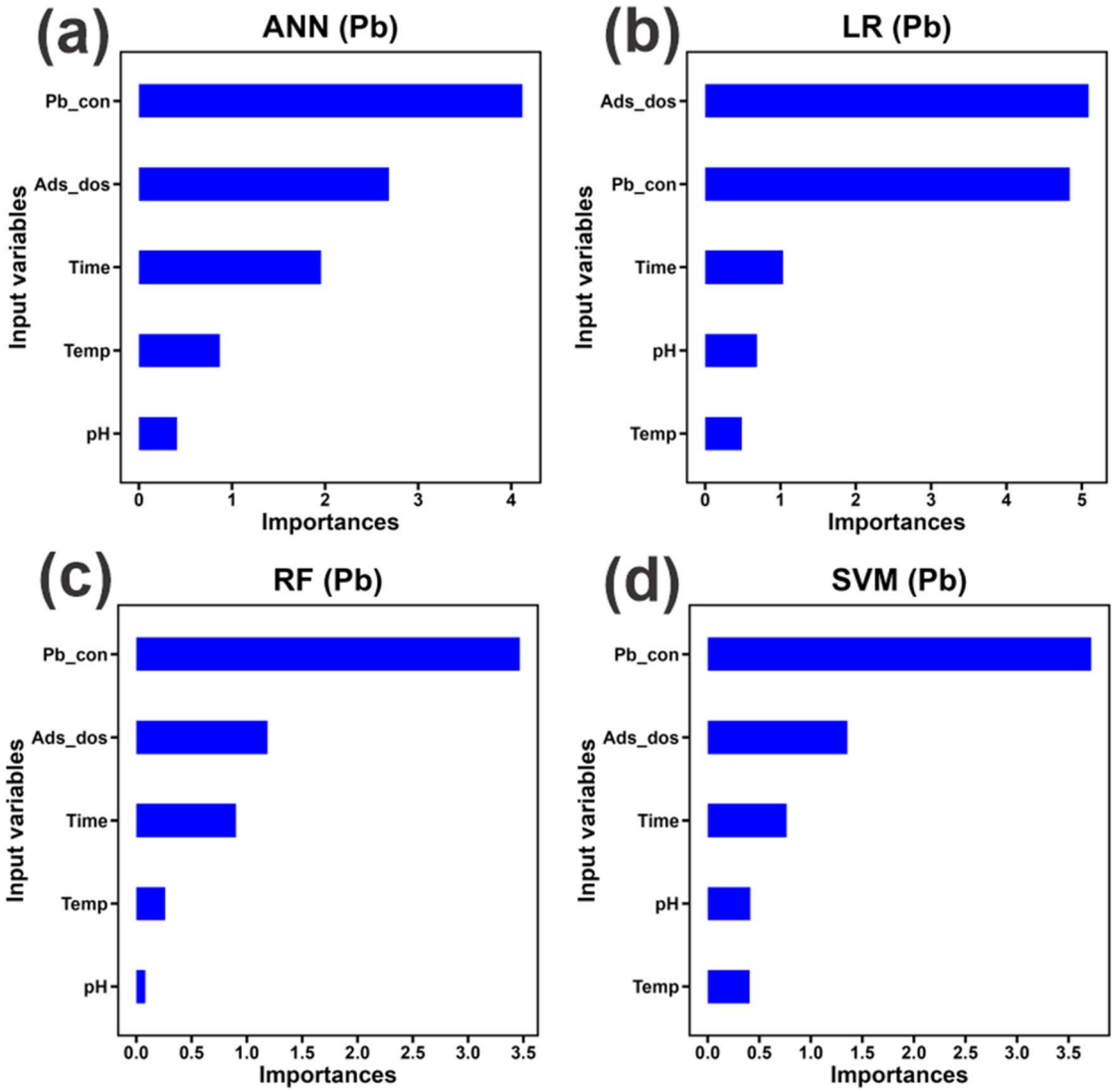


Fig. 11 The prediction of Importance plot: ANN (a); LR (b); RF (c); SVM (d) for Pb adsorption capacity by CGW.

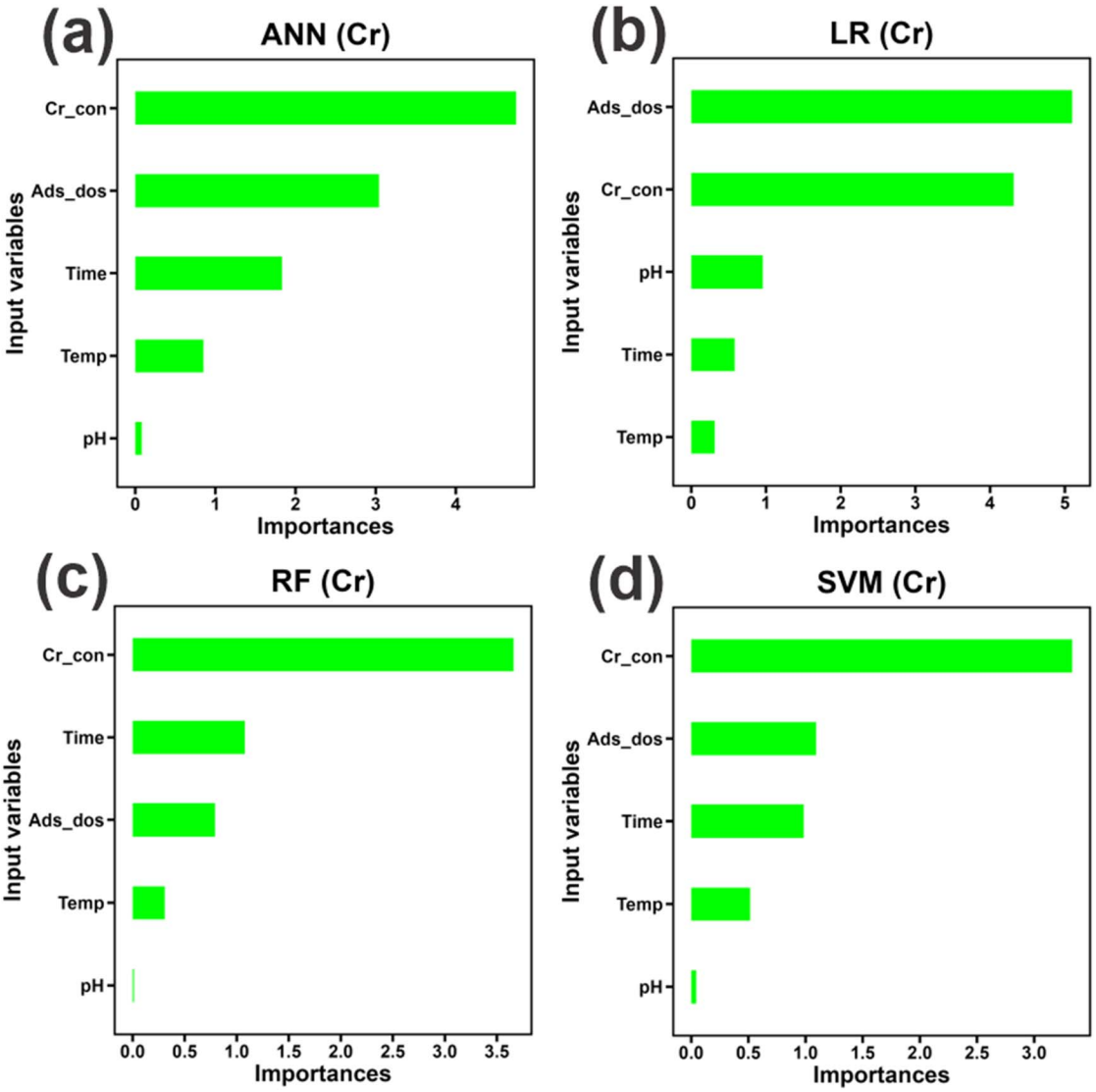


Fig. 12 The prediction of Importance plot: ANN (a); LR (b); RF (c); SVM (d) for Cr adsorption capacity by CGW.

driven physisorption predominates, while Cr(VI) is more sensitive to pH-mediated chemisorption, supporting the multi-mechanism framework proposed earlier. By integrating these ML predictions, future process designs can optimize parameters such as dosage and pH to maximize efficiency, promoting sustainable textile waste valorization and advancing circular economy principles in environmental engineering.

**Mechanism of Pb and Cr adsorption using CGW.** To elucidate the adsorption mechanisms governing simultaneous Pb(II) and Cr(VI) removal, structural and surface characteristics of CGW600 before and after adsorption were systematically compared using EDX, XRD, and FTIR analyses (Fig. 3–5 and S2). This comparison provides direct experimental evidence supporting the proposed mechanisms and allows differentiation between dominant and secondary processes.

Anaerobic pyrolysis induces a temperature-dependent evolution in the morphology and surface chemistry of CGW. At moderate carbonization (CGW600), the fibrous textile-derived structure transforms into a heterogeneous porous carbon matrix with the highest BET surface area (56.85 $m^2 g^{-1}$) and pore volume (0.046 $cm^3 g^{-1}$), providing abundant accessible adsorption sites. SEM observations confirm the development of fractured carbon domains and mesoporous structures, while XRD patterns indicate predominantly amorphous carbon with moderate aromatic ordering, which enhances site accessibility without the pore densification observed at 900 °C.

The EDX spectrum of pristine CGW600 (Fig. 2) is dominated by C and O, with minor mineral elements originating from the textile matrix. After adsorption (Fig. S3a), distinct Pb and Cr peaks emerge, confirming the successful immobilization of both metals on the biochar surface. The presence of these elements together with slight variations in oxygen-containing components suggests that adsorption involves interaction with surface functional groups rather than simple physical deposition. This observation provides direct evidence for surface complexation and ion-exchange processes, particularly

 

for Pb(II), which preferentially binds to oxygen-containing functional groups such as hydroxyl and carbonyl groups.

XRD patterns further clarify structural stability and metal retention pathways. The pristine CGW600 exhibits a broad diffraction peak at $2\theta \approx 24$–$26°$ (Fig. 3), characteristic of amorphous carbon. After adsorption (Fig. S3b), the overall amorphous structure remains largely unchanged, indicating that the carbon matrix maintains structural integrity during metal uptake. Minor changes in peak intensity and weak additional reflections suggest surface coordination or limited precipitation of metal-associated phases. The absence of sharp crystalline peaks corresponding to bulk Pb or Cr oxides indicates that large-scale crystallization is unlikely, and that metals are primarily retained *via* surface binding and dispersion within the pore structure. Therefore, precipitation-driven mechanisms are considered secondary rather than dominant.

FTIR spectra provide further evidence for functional group involvement. Comparison of spectra before adsorption (Fig. 4) and after adsorption (Fig. S3c) reveals shifts and intensity reductions in bands corresponding to –OH (~3400 $cm^{-1}$), C=O (~1700 $cm^{-1}$), and C–O/C–N (~1000–1300 $cm^{-1}$). These changes indicate direct interaction between metal species and surface functional groups. The attenuation and shift of these bands support the formation of surface complexes and possible ion exchange between metal ions and functional groups on the biochar surface. Such evidence strongly supports surface complexation as a dominant adsorption pathway for Pb(II).[49,53]

Pb(II) adsorption onto CGW is dominated by electrostatic attraction and inner-sphere surface complexation, particularly at the selected operational pH of 7. At near-neutral pH, partial deprotonation of carboxylic and phenolic groups generates negatively charged sites.[63] These sites strongly coordinate $Pb^{2+}$ ions, forming surface complexes such as:

$$CGW - COO^- + Pb^{2+} \rightarrow CGW - COO - Pb^+ \quad (10)$$

or bidentate inner-sphere complexes:

$$2(CGW - O^-) + Pb^{2+} \rightarrow (CGW - O)_2Pb \quad (11)$$

This mechanism is consistent with the experimentally observed increase in Pb(II) adsorption capacity from 3.38–5.40 mg $g^{-1}$ at pH 3 to 6.82–7.64 mg $g^{-1}$ at pH 7, as well as with the excellent fit of the pseudo-first-order kinetic model ($k_1$ = 0.0588 $min^{-1}$ for CGW600), indicating that surface-site availability and mass transfer dominate Pb uptake rather than precipitation processes.[44]

Additionally, ion exchange contributes to Pb immobilization, whereby $Pb^{2+}$ displaces weakly bound alkaline or alkaline-earth cations (*e.g.*, $Ca^{2+}$, $K^+$) detected by EDX:

$$CGW - Ca^{2+} + Pb^{2+} \rightarrow CGW - Pb^{2+} + Ca^{2+} \quad (12)$$

The Sips isotherm model ($q_m$ = 19.56 mg $g^{-1}$, $n$ = 0.555 for CGW600) further confirms adsorption on energetically heterogeneous surfaces, involving a combination of functional-group binding and pore filling within mesopores (average pore size ≈ 3.21 nm). Similar mechanistic pathways have been reported for Pb(II) adsorption on oxygen-rich biochars derived from agricultural and textile wastes.[64]

In contrast to Pb(II), Cr(VI) exists predominantly as anionic species ($CrO_4^{2-}$ and $HcrO_4^-$) at pH 7, rendering electrostatic attraction to negatively charged CGW surfaces unfavorable. Nevertheless, substantial Cr removal is achieved, indicating that Cr(VI) adsorption proceeds *via* a coupled adsorption–reduction–immobilization mechanism rather than simple electrostatic binding.[65]

Initially, Cr(VI) interacts with neutral or weakly protonated surface sites and defect-rich aromatic domains through specific adsorption and hydrogen bonding.[63] Subsequently, partial reduction of Cr(VI) to Cr(III) occurs *via* electron donation from surface functional groups and the conjugated carbon matrix:

$$CrO_42- + 3e^- + 8H^+ \rightarrow Cr^{3+} + 4H_2O \quad (13)$$

Although bulk solution pH is neutral, localized acidic microenvironments near surface functional groups facilitate this reduction process, as reported for numerous biochar systems. The generated Cr(III) species are then immobilized through surface complexation or precipitation:

$$CGW - COO^- + Cr^{3+} \rightarrow CGW - COO - Cr^{2+} \quad (14)$$

$$Cr^{3+} + 3OH^- \rightarrow Cr(OH)_3\downarrow \quad (15)$$

This mechanism explains the sustained Cr(VI) adsorption at pH 7 and is consistent with the superior fit of the Sips isotherm ($q_m$ = 18.19 mg $g^{-1}$ for CGW600) and pseudo-first-order kinetics, reflecting heterogeneous surface reactions coupled with diffusion-controlled uptake. Similar redox-assisted Cr(VI) removal mechanisms have been extensively documented for biochar-based adsorbents.[45,54]

One of the most notable findings of this study is the effective simultaneous removal of Pb(II) and Cr(VI) at pH 7 using CGW600, which is more representative of practical wastewater treatment conditions than the strongly acidic environments typically required for efficient Cr(VI) removal in many reported systems. The favorable performance under near-neutral conditions can be attributed to the balanced physicochemical properties of CGW600, produced at a moderate carbonization temperature, which preserve both the pore structure and surface functional groups. Oxygen-containing functional groups identified by FTIR provide active binding sites for Pb(II) through surface complexation and ion exchange. In contrast, the heterogeneous surface chemistry and residual mineral components facilitate Cr(VI) retention through a combination of adsorption, localized electrostatic interactions, and possible redox-assisted immobilization. The coexistence of diverse functional groups and accessible pore structures enables parallel adsorption pathways for both cationic Pb(II) and anionic chromate species, reducing competitive inhibition during co-adsorption. This multifunctional surface environment explains the effective Pb–Cr removal at neutral pH. It highlights the practical applicability of textile waste-derived biochar for real wastewater treatment, where operation under

near-neutral conditions is preferred to minimize chemical consumption and operational complexity.

Beyond predictive accuracy, the ML analysis provides additional scientific insight into the governing factors controlling the simultaneous adsorption of Pb(II) and Cr(VI). Variable-importance evaluations from the ANN, RF, and SVM models consistently identify pH, adsorbent dosage, and initial metal concentration as the most influential parameters affecting adsorption performance. This finding is mechanistically meaningful rather than purely statistical. The dominant role of pH revealed by the ML models is consistent with the experimentally observed dependence of adsorption on surface charge conditions, metal speciation, and protonation–deprotonation behavior of functional groups. Similarly, the strong influence of adsorbent dosage reflects the availability of active binding sites and the accessibility of pores, supporting the proposed roles of surface complexation and pore-filling mechanisms. The importance of initial metal concentration further indicates that adsorption capacity is governed by the balance between available functional groups and competitive occupation of heterogeneous surface sites during simultaneous Pb–Cr removal. The ML results clarify the relative contributions of different mechanisms by quantitatively confirming that adsorption performance is primarily controlled by surface chemistry and site availability rather than by structural transformations or precipitation processes. This interpretation aligns with the spectroscopic and structural evidence discussed above, which indicates that functional group interactions and dispersed surface binding dominate over bulk crystalline phase formation. Therefore, the ML analysis complements and extends the experimental findings by providing a quantitative framework that links operational parameters to underlying adsorption mechanisms. Rather than serving solely as predictive tools, the ML models strengthen mechanistic interpretation by identifying the controlling variables governing simultaneous heavy metal removal under near-neutral conditions. These findings align closely with recent ML-based mechanistic studies on heavy metal adsorption by biochars.[66]

Therefore, CGW600 provides an optimal balance between surface functionality, porosity, and structural stability, enabling efficient simultaneous removal of Pb(II) and Cr(VI) at pH 7. Pb(II) is primarily immobilized *via* electrostatic attraction, surface complexation, and ion exchange, whereas Cr(VI) removal proceeds through specific adsorption coupled with partial reduction to Cr(III) and subsequent stabilization. The convergence of experimental modeling and ML analysis confirms that adsorption on CGW is inherently heterogeneous and multi-mechanistic, making CGW600 a promising, sustainable adsorbent for treating mixed-metal textile wastewater.

Table 5 compares the Pb(II) and Cr(VI) adsorption performance of CGW600 with that of representative biochar- and carbon-based adsorbents reported in the literature. Many high-capacity systems rely on strong chemical activation or functional composite design, such as KOH-activated biochar, which achieves Langmuir capacities of 140.0 mg $g^{-1}$ for Pb(II) and 127.2 mg $g^{-1}$ for Cr(VI) at their respective optimum pH values. Likewise, engineered composites (*e.g.*, FeS/chitosan/biochar or magnetic biochars) frequently show enhanced Cr(VI) uptake (80–104 mg $g^{-1}$), but typically under acidic conditions and with material complexity that may limit scalability.[73] In contrast, many biomass-derived biochars that target a single metal report high Pb(II) adsorption only when pH is tuned and/or the feedstock is mineral-rich.[49] A key strength of the present study is the effective simultaneous removal of Pb(II) and Cr(VI) at pH 7, which is closer to practical wastewater conditions and avoids intensive pH adjustment. At neutral pH, Pb(II) can be

Table 5 Comparison of reported adsorption capacities for Pb(II) and Cr(VI) using biochar/carbon-based adsorbents

| No. | Adsorbent | Target | Optimum pH | Capacity Pb(II) (mg $g^{-1}$) | Capacity Cr(VI) (mg $g^{-1}$) | System type | References |
|---|---|---|---|---|---|---|---|
| 1 | CGW600 (garment waste biochar) | Pb + Cr | 7 | 23.18 | 19.68 | Multi-metal simultaneous | This work |
| 2 | KOH-activated Douglas fir biochar | Pb + Cr | "pH of maximum adsorption" | 140.0 | 127.2 | Single-metal | 67 |
| 3 | Cassava root husk biochar loaded with ZnO NPs | Pb + Cr(VI) (+others) | 6–7 | 44.27 | 28.37 | Multi-metal simultaneous | 68 |
| 4 | Hybrid biochar from biomass + plastic waste | Pb + Cr(VI) | — | 15.22 | 36.63 | Multi-metal simultaneous | 69 |
| 5 | Corncob biochar | Cr(VI) | 2.0 | — | 38.1 | Single-metal | 50 |
| 6 | Spent mushroom substrate biochar | Pb(II) | 2–6 | 326 (PC700)/398 (SC700) | — | Single-metal | 49 |
| 7 | Modified atermelon seed biochar | Pb(II) | pH varied | 60.87 | — | Single-metal | 70 |
| 8 | Corn stalk biochar | Pb(II) | 5.5 | 124.7 | — | Single-metal | 71 |
| 9 | $Fe_3O_4$@$SiO_2$–$NH_2$ modified biochar (magnetic) | Cr(VI) | Acidic favored | — | 27.2 | Single-metal | 72 |
| 10 | FeS/chitosan/biochar composite | Cr(VI) | pH affects strongly | — | 103.93 | Single-metal | 73 |
| 11 | Magnetic biochar adsorbents | Cr(VI) | — | — | 80.96 | Single-metal | 74 |

immobilized *via* surface complexation/ion exchange with oxygen-containing functional groups, whereas Cr(VI) removal is often challenging because chromate species remain anionic and electrostatic attraction is weakened. The ability of CGW600 to remove both species concurrently at pH 7 suggests that its heterogeneous surface chemistry and pore structure provide parallel uptake pathways for cationic and anionic contaminants, enabling practical co-removal without extreme pH control. Compared with other multi-metal studies (*e.g.*, cassava root husk biochar loaded with ZnO nanoparticles), which typically report optimum performance around pH 6–7 but often involve multiple metals and engineered additives, CGW600 offers a simpler, textile-waste-derived route while maintaining competitive capacities for both Pb and Cr under neutral conditions.[68]

**Practical implications and trade-offs between fuel and adsorption functions.** The results clearly demonstrate that carbonization temperature plays a decisive role in determining whether carbonized garment waste (CGW) is better suited for fuel applications or for adsorption-based remediation. Biochars produced at higher temperatures (800–900 °C) exhibit superior fuel-related properties, including higher fixed carbon content, higher calorific value, and improved combustion stability. In contrast, biochar produced at a moderate temperature (600 °C) retains a more developed pore structure and higher density of surface functional groups, resulting in enhanced adsorption performance for Pb(II) and Cr(VI).

From a practical perspective, these findings indicate that a single biochar batch cannot simultaneously maximize both fuel efficiency and adsorption capacity. This reflects an inherent trade-off between carbon structural ordering required for energy applications and surface functionality required for adsorption. Nevertheless, the production framework remains practically viable, as textile waste-derived biochar can be selectively tailored toward either energy recovery or wastewater remediation by adjusting carbonization temperature. Such flexibility enables application-specific optimization within a unified waste valorization strategy rather than requiring a one-size-fits-all material.

## Conclusion

This study demonstrates the effective valorization of post-industrial garment waste into a multifunctional biochar *via* anaerobic pyrolysis, providing a unified approach that integrates waste-to-energy recovery with wastewater remediation. The results clearly show that the carbonization temperature governs the multifunctional performance of the resulting material, resulting in a measurable trade-off between fuel-related properties and adsorption capacity. Biochar produced at high temperatures (800–900 °C) exhibited excellent fuel characteristics, including high carbon content (>76 wt%), low ash (<1.4 wt%), and high calorific values (6906–7069 kcal $kg^{-1}$), achieving thermal efficiencies of approximately 70% in practical water-boiling tests. These values are comparable to or higher than those of conventional coal briquettes, confirming the suitability of high-temperature CGW as a sustainable solid fuel.

In contrast, CGW600 demonstrated optimal adsorption performance, with maximum Langmuir capacities of 23.18 mg $g^{-1}$ for Pb(II) and 19.68 mg $g^{-1}$ for Cr(VI), outperforming the other CGW samples due to its higher surface area (56.85 $m^2 g^{-1}$) and pore volume (0.046 $cm^3 g^{-1}$). Notably, simultaneous Pb–Cr removal was achieved at pH 7 with equilibrium adsorption capacities of 9.43 ± 0.26 mg $g^{-1}$ for Pb(II) and 8.78 ± 0.18 mg $g^{-1}$ for Cr(VI), demonstrating effective co-removal under near-neutral conditions that are more relevant to real wastewater treatment than the strongly acidic conditions typically required for Cr(VI) adsorption. Compared with many reported biochar-based systems that require separate optimization conditions for cationic and anionic metals, the present CGW600 system enables efficient dual-metal removal within a single operational window.

Mechanistic analysis, supported by FTIR, XRD, EDX, and adsorption modeling, indicates that Pb(II) uptake is primarily governed by surface complexation and ion exchange, whereas Cr(VI) removal involves adsorption coupled with redox-assisted immobilization. Machine learning analysis further revealed that pH, adsorbent dosage and initial concentration are the dominant factors controlling adsorption performance, providing quantitative confirmation of the experimental findings and offering a predictive framework for process optimization.

The novelty of this study lies in the integrated evaluation of garment waste-derived biochar as both a solid fuel and a dual-metal adsorbent, together with machine-learning-assisted interpretation of adsorption behavior. Unlike most previous studies that focus on a single functionality, this work establishes a practical temperature-dependent framework for tailoring biochar toward either energy recovery or environmental remediation. The findings highlight the feasibility of converting textile waste into value-added carbon materials that address both solid waste management and the treatment of heavy-metal-contaminated wastewater. From a practical standpoint, optimizing the carbonization temperature enables flexible deployment of CGW as either a clean-burning household fuel or an effective adsorbent operating under near-neutral conditions, thereby supporting circular economy strategies in textile-producing regions.

This study confirms the existence of a temperature-dependent trade-off between fuel performance and the adsorption capacity of garment waste-derived biochar. While a single biochar cannot simultaneously optimize both functions, controlled carbonization enables flexible, application-oriented utilization within an integrated textile waste valorization framework.

## Author contributions

Thu Huong Nguyen, Trung Kien Hoang conceived, planned and carried out experiments; Huu-Tap Van carried out experiments; Thi Minh Phuong Nguyen contributed to the interpretation of the results; Huu-Tap Van, Thi Minh Phuong wrote the manuscript.

## Conflicts of interest

The authors have not disclosed any competing interests.

## Data availability

Data associated with this study has not been deposited into a publicly available repository. Data will be made available on request.

Supplementary information (SI) is available. See DOI: https://doi.org/10.1039/d6ra00384b.

## Acknowledgements

This work was financially supported by Vietnam Ministry of Education and Training under project number: B2024-TNA-07.

## References

1 G. Sandin and G. M. Peters, *J. Cleaner Prod.*, 2018, **184**, 353–365.
2 K. Niinimäki, G. Peters, H. Dahlbo, P. Perry, T. Rissanen and A. Gwilt, *Nat. Rev. Earth Environ.*, 2020, **1**, 189–200.
3 H. Xi, Z. Li, J. Han, D. Shen, N. Li, Y. Long, Z. Chen, L. Xu, X. Zhang, D. Niu and H. Liu, *Waste Manage.*, 2022, **139**, 208–216.
4 Z. H. Mussa, A. F. Imran, L. R. Al-Ameer, H. F. S. Al-Saedi, I. F. Deyab, F. F. A-Qaim and H. Kamyab, *Results Surf. Interfaces*, 2025, **20**, 100618.
5 F. K. Shooshtari, M. S. Mohtaram, P. Roohparvarzadeh, M. M. Zerafat, H. Kamyab, H. Moradi, S. Rajendran and S. Sabbaghi, *J. Water Process Eng.*, 2025, **79**, 108953.
6 H. Kamyab, S. Chelliapan, E. Khalili, S. Rezania, B. Balasubramanian, M. M. Taheri, D. Simancas-Racines, S. Rajendran and M. Yusuf, *J. Hazard. Mater. Adv.*, 2025, **18**, 100673.
7 H. Kamyab, S. Chelliapan, E. Khalili, D. P. Z. Mediavilla, M. Khorami, T. M. Aminabhavi and Y. Vasseghian, *J. Environ. Manage.*, 2025, **392**, 126736.
8 N. Bolan, S. A. Hoang, J. Beiyuan, S. Gupta, D. Hou, A. Karakoti, S. Joseph, S. Jung, Ki-H. Kim, M. B. Kirkham, H. W. Kua, M. Kumar, E. E. Kwon, Y. Sik Ok, V. Perera, J. Rinklebe, S. M. Shaheen, B. Sarkar, A. K. Sarmah, B. P. Singh, G. Singh, D. C. W. Tsang, K. Vikrant, M. Vithanage, A. Vinu, H. Wang, H. Wijesekara, Y. Yan, S. A. Younis and L. Van Zwieten, *Int. Mater. Rev.*, 2022, **67**, 150–200.
9 J. Wang and S. Wang, *J. Cleaner Prod.*, 2019, **227**, 1002–1022.
10 G. Crini and E. Lichtfouse, *Environ. Chem. Lett.*, 2019, **17**, 145–155.
11 F. Fu and Q. Wang, *J. Environ. Manage.*, 2011, **92**, 407–418.
12 G. Crini and E. Lichtfouse, *Environ. Chem. Lett.*, 2019, **17**, 145–155.
13 J. Zhou, Z. Lou, J. Xu, X. Zhou, K. Yang, X. Gao, Y. Zhang and X. Xu, *Chem. Eng. J.*, 2019, **358**, 1176–1185.
14 S. Yu, Y. Gao, X. Zhu, H. Yu, Y. Zhang and J. Chen, *Sci. Total Environ.*, 2023, **858**, 159875.
15 M. E. Boesch, C. Vadenbo, D. Saner, C. Huter and S. Hellweg, *Waste Manage.*, 2014, **34**, 378–389.
16 W. Hu, X. Zhang, M. Chen, S. T. Rahman, X. Li and G. Wang, *Molecules*, 2024, **29**, 2220.
17 T. N. Huynh, D. T. Nguyen, H. H. Phuong Uyen Pham, A. D. Trinh and Q. H. Tran, *RSC Adv.*, 2026, **16**, 2767–2782.
18 Y. Zhu, F. Gao, L. Yi, H. Yi, Q. Yu, S. Zhao, Y. Zhou, Y. Wang and X. Tang, *Appl. Energy*, 2025, **396**, 126241.
19 J. Huang, Y. Jian, H. Li and Z. Fang, *Catal. Today*, 2022, **404**, 35–48.
20 J. Huang, T. Liu, K. Wang, Z. Huang, J. Wang, S. L. Rokhum and H. Li, *Environ. Chem. Lett.*, 2024, **22**, 1607–1613.
21 H. T. Van, T. C. Luu, V. H. Hoang, T. L. Vi, T. H. Nguyen, T. K. Hoang, T. B. L. Nguyen, H. Nguyen, T. H. Dam, D. H. Lu, A. Dia Thao and L. H. Nguyen, *RSC Adv.*, 2025, **15**, 30360–30377.
22 Y.-G. Kang, D.-G. Park, J.-Y. Lee, J. Choi, J.-H. Kim, J.-H. Kim, Y.-U. Yun and T.-K. Oh, *Sci. Rep.*, 2024, **14**, 29910.
23 X. Gai, H. Wang, J. Liu, L. Zhai, S. Liu, T. Ren and H. Liu, *PLoS One*, 2014, **9**, e113888.
24 W. Xiang, X. Zhang, J. Chen, W. Zou, F. He, X. Hu, D. C. W. Tsang, Y. S. Ok and B. Gao, *Chemosphere*, 2020, **252**, 126539.
25 J. Chang, S. Yü, Y. Liao, X. Guan, H. Gao and Y. Li, *ACS Omega*, 2022, **7**, 42854–42864.
26 J.-P. Simonin, *Chem. Eng. J.*, 2016, **300**, 254–263.
27 R. B. Fidel, D. A. Laird and K. A. Spokas, *Sci. Rep.*, 2018, **8**, 1–10.
28 M. Moradi, Y. Vasseghian, H. Arabzade and A. Mousavi Khaneghah, *Chemosphere*, 2021, **263**, 128314.
29 W. Li, C. H. Luna-Flores, R. Anangi, R. Zhou, X. Tan, M. Jessen, L. Liu, R. Zhou, T. Zhang, A. Gissibl, P. J. Cullen, K. (Ken) Ostrikov and R. E. Speight, *Bioresour. Technol.*, 2023, **369**, 128370.
30 T. Li, M. Wu, C. Duan, S. Li and C. Liu, *Sci. Total Environ.*, 2022, **806**, 150626.
31 H. Ren, J. Jiang, D. Wu, Z. Gao, Y. Sun and C. Luo, *Water, Air, Soil Pollut.*, 2016, **227**, 101–122.
32 Z. Li, H. Chen, L. Zhan, S. Zheng and L. Yang, *Fuel Process. Technol.*, 2023, **245**, 107697.
33 A. Domene, H. Orozco, P. Rodríguez-Viso, V. Monedero, M. Zúñiga, D. Vélez and V. Devesa, *Environ. Res.*, 2024, **245**, 117989.
34 A. Domene, H. Orozco, P. Rodríguez-Viso, V. Monedero, M. Zúñiga, D. Vélez and V. Devesa, *Environ. Res.*, 2024, **245**, 117989.
35 W. Li, C. H. Luna-Flores, R. Anangi, R. Zhou, X. Tan, M. Jessen, L. Liu, R. Zhou, T. Zhang, A. Gissibl, P. J. Cullen, K. (Ken) Ostrikov and R. E. Speight, *Bioresour. Technol.*, 2023, **369**, 128370.
36 A. T. Sipra, N. Gao and H. Sarwar, *Fuel Process. Technol.*, 2018, **175**, 131–147.
37 S. Barışçı and M. S. Öncel, *Int. J. Green Energy*, 2014, **11**, 255–266.
38 Y. Wu, C. Wen, X. Chen, G. Jiang, G. Liu and D. Liu, *Fuel Process. Technol.*, 2017, **166**, 115–123.

39 V. Stamatov, D. Honnery and J. Soria, *Renewable Energy*, 2006, **31**, 2108–2121.
40 C. Balcik-Canbolat, B. Ozbey, N. Dizge and B. Keskinler, *Int. J. Green Energy*, 2016, **14**, 289–294.
41 A. Khoirul Anas, A. Izzah, S. Pratama and F. Fajarwati, *AIP Conf. Proc.*, 2020, **2229**, e030024.
42 I. Pitak and A. Sholokhova, *Clean. Waste Syst.*, 2025, **10**, 100199.
43 E. Yáñez, A. Ramírez, A. Uribe, E. Castillo and A. Faaij, *J. Cleaner Prod.*, 2018, **176**, 604–628.
44 J. Wu, T. Wang, Y. Zhang and W. P. Pan, *Bioresour. Technol.*, 2019, **291**, 121859.
45 J. T. Padilla, D. W. Watts, A. A. Szogi and M. G. Johnson, *Chemosphere*, 2024, **347**, 140688.
46 X. Wang, Q. Chi, X. Liu and Y. Wang, *Chemosphere*, 2019, **216**, 698e706.
47 Y. Alvarez-Galvan, B. Minofar, Z. Futera, M. Francoeur, C. Jean-Marius, N. Brehm, C. Yacou, U. J. Jauregui-Haza and S. Gaspard, *Molecules*, 2022, **27**, 6040.
48 E. D. Revellame, D. L. Fortela, W. Sharp, R. Hernandez and M. E. Zappi, *Clean. Eng. Technol.*, 2020, **1**, 100032.
49 Q. Wu, Y. Xian, Z. He, Q. Zhang, J. Wu, G. Yang, X. Zhang, H. Qi, J. Ma, Y. Xiao and L. Long, *Sci. Rep.*, 2019, **9**, 15999.
50 D.-K. Nguyen, Q.-B. Ly-Tran, V.-P. Dinh, B.-N. Duong, T.-P.-T. Nguyen and P. Nguyen Kim Tuyen, *RSC Adv.*, 2024, **14**, 39205–39218.
51 M. Shafiq, A. A. Alazba and M. T. Amin, *Sustainability*, 2021, **13**, 3785.
52 P. Kumkum and S. Kumar, *Biomass*, 2024, **4**, 243–272.
53 S. Wang, J.-H. Kwak, M. S. Islam, M. A. Naeth, M. Gamal El-Din and S. X. Chang, *Sci. Total Environ.*, 2020, **712**, 136538.
54 L. Yan, F.-X. Dong, X. Lin, X.-H. Zhou, L.-J. Kong, W. Chu and Z.-H. Diao, *Environ. Technol. Innovation*, 2021, **24**, 102057.
55 M. Esfandyari, M. Khodadadi, R. N. Ghadirli and D. Jafari, *Desalin. Water Treat.*, 2022, **252**, 167–176.
56 T. Salazar-Rojas, F. R. Cejudo-Ruiz and G. Calvo-Brenes, *Environ. Pollut.*, 2022, **314**, 120227.
57 N. Parveen, S. Zaidi and M. Danish, *Process Saf. Environ. Prot.*, 2017, **107**, 428–437.
58 A. El Hanandeh, Z. Mahdi and M. S. Imtiaz, *Environ. Res.*, 2021, **192**, 110338.
59 T. Shen, H. Peng, X. Yuan, Y. Liang, S. Liu, Z. Wu, L. Leng and P. Qin, *J. Hazard. Mater.*, 2024, **466**, 133442.
60 Z. M. Yaseen and F. L. Alhalimi, *Sci. Rep.*, 2025, **15**, 13434.
61 T. Salazar-Rojas, F. R. Cejudo-Ruiz and G. Calvo-Brenes, *Environ. Pollut.*, 2022, **314**, 120227.
62 M. Esfandyari, M. Khodadadi, R. N. Ghadirli and D. Jafari, *Desalin. Water Treat.*, 2022, **252**, 167–176.
63 Y. Yu, J. He, J. Sun, Z. Pei, Q. Wu and R. Yu, *Sustainability*, 2023, **15**, 7627.
64 T. Chen, L. Xing and S. Niu, *Diamond Relat. Mater.*, 2024, **148**, 111353.
65 T. Chen, L. Xing and S. Niu, *Diamond Relat. Mater.*, 2024, **148**, 111353.
66 X. Wei, Y. Liu, L. Shen, Z. Lu, Y. Ai and X. Wang, *Biochar*, 2024, **6**, 10.
67 A. Herath, C. A. Layne, F. Perez, E. I. B. Hassan, C. U. Pittman and T. E. Mlsna, *Chemosphere*, 2021, **269**, 128409.
68 P. T. Tho, H. T. Van, L. H. Nguyen, T. K. Hoang, T. N. Ha Tran, T. T. Nguyen, T. B. Hanh Nguyen, V. Q. Nguyen, H. Le Sy, V. N. Thai, Q. B. Tran, S. M. Sadeghzadeh, R. Asadpour and P. Q. Thang, *RSC Adv.*, 2021, **11**, 18881–18897.
69 E. C. Emenike, H. K. Okoro, G. M. Al-Senani, S. D. Al-Qahtani, K. O. Iwuozor, A. U. Egbemhenghe, J. Emeghai and A. G. Adeniyi, *Biomass Bioenergy*, 2026, **207**, 108722.
70 W. Ahmed, S. Mehmood, A. Núñez-Delgado, S. Ali, M. Qaswar, A. Shakoor, M. Mahmood and D.-Y. Chen, *Sci. Total Environ.*, 2021, **784**, 147136.
71 W. Yang, C. Lu, B. Liang, C. Yin, G. Lei, B. Wang, X. Zhou, J. Zhen, S. Quan and Y. Jing, *Separations*, 2023, **10**, 438.
72 S. Shi, J. Yang, S. Liang, M. Li, Q. Gan, K. Xiao and J. Hu, *Sci. Total Environ.*, 2018, **628–629**, 499–508.
73 Y. Yang, Y. Zhang, G. Wang, Z. Yang, J. Xian, Y. Yang, T. Li, Y. Pu, Y. Jia, Y. Li, Z. Cheng, S. Zhang and X. Xu, *J. Environ. Chem. Eng.*, 2021, **9**, 105407.
74 C. Santhosh, E. Daneshvar, K. M. Tripathi, P. Baltrėnas, T. Y. Kim, E. Baltrėnaitė and A. Bhatnagar, *Environ. Sci. Pollut. Res.*, 2020, **27**, 32874–32887.